#### **ORIGINAL PAPER**



# Common assumptions and methods yield overestimated diffusive timescales, as exemplified in a Yellowstone post-caldera lava

Kara Brugman<sup>1,2</sup> • Christy B. Till<sup>1</sup> • Maitrayee Bose<sup>1</sup>

Received: 17 September 2021 / Accepted: 24 May 2022 © The Author(s), under exclusive licence to Springer-Verlag GmbH Germany, part of Springer Nature 2022

#### Abstract

To interpret modern-day unrest at Yellowstone Caldera, timescales leading up to its most common type of eruption—effusively emplaced rhyolite—must be quantified. This work takes advantage of the different rates of elemental diffusion in clinopyroxene to calculate the magmatic timescales of events preceding eruption of the ca. 262 ka Scaup Lake rhyolite, which ended ~ 220,000 years of dormancy in this high-silica system. Here, we present diffusion chronometry timescales accounting for various sources of error and using multiple elements from NanoSIMS measurements of clinopyroxene rims. We combine these with previously published timescales from sanidine rims to better understand the relationship between timescales captured by different minerals from the same volcanic event. We show that timescales archived by rims of different types of phenocrysts from the same lava may not be concomitant. The Scaup Lake rhyolite appears to have undergone several rejuvenation events over ~ 5000 years before its eruption, and the last events (< 40 years before eruption) were not recorded by clinopyroxene. This work highlights the importance of using multiple methods to determine a timescale for a given process. Although many studies use Fe-Mg zonation from BSE images to calculate diffusive timescales alone, we show that these are maximums or overestimates if not referenced to the appropriate initial condition. Instead, we demonstrate that diffusion chronometry conducted with multiple elements in multiple mineral phases with rigorous error propagation produces the most robust and accurate temporal results. In addition, we recommend that diffusion chronometry results not be interpreted in isolation, but rather in a holistic petrological approach that includes consideration of the relevant phase equilibria and crystal growth and dissolution rates.

Keywords Yellowstone · Diffusion chronometry · Clinopyroxene · Rhyolite · Sanidine · Initial condition

#### Introduction

A persistent challenge in the study of volcanoes and their magmatic systems is determining timescales of magmatic processes. In part, the goal of such research is to construct a timeline of pre-eruptive events that may be used to forecast volcanic eruptions. Geochemical studies have investigated the rate and duration of various magmatic processes, including residence time of a crystal in a magma (Bindeman

Communicated by Mark S Ghiorso.

 ⊠ Kara Brugman kbrugman@carnegiescience.edu

Published online: 21 June 2022

- School of Earth and Space Exploration, Arizona State University, Tempe, AZ, USA
- Earth & Planets Laboratory, Carnegie Institution for Science, Washington, DC, USA

and Valley 2001; Morgan et al. 2004; Wotzlaw et al. 2015), magma chamber assembly (Druitt et al. 2012; Rubin et al. 2016; Reid and Vazquez 2017), magma generation and reheating rates (Bachmann and Bergantz 2006; Simakin and Bindeman 2012), timescales of intrusion and ascent rates (Myers et al. 2016; Moussallam et al. 2019; Newcombe et al. 2020), rejuvenation (Costa and Chakraborty 2004; Martin et al. 2008; Hartley et al. 2016; Pistone et al. 2017), assimilation (Costa and Dungan 2005), and pre-eruptive "priming" (Stock et al. 2016; Petrone et al. 2018). In recent years, the application of diffusion chronometry to these investigations has flourished. Diffusion chronometry employs the rate at which elements migrate through the mineral to attain chemical equilibrium (Costa and Morgan 2011). Timescales determined using this method represent the amount of time that has elapsed between when a chemically distinct mineral zone grew and when the mineral cooled enough to halt chemical diffusion—in magmatic systems, this occurs when

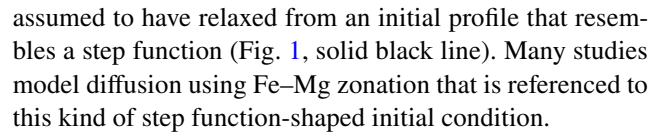


the mineral cools after volcanic emplacement, although quantifiable diffusion may continue in the hot interiors of lava flows and domes (e.g., Couperthwaite et al. 2021). This method has been used to study many magmatic systems from mafic to silicic, and the calculated timescales can be as short as days to weeks (e.g., Pamukcu et al. 2016; Mutch et al. 2019; Morgado et al. 2019; Sundermeyer et al. 2020; Costa et al. 2020; Prissel et al. 2020; Kent et al. 2020).

Most studies of intracrystalline diffusion in magmatic systems employ a single element in one mineral, while a fraction use diffusion timescales from different elements within a given mineral (e.g., Costa and Dungan 2005; Morgan and Blake 2006; Druitt et al. 2012; Till et al. 2015; Albert et al. 2015, 2019; Bouvet de Maisonneuve et al. 2016; Lynn et al. 2017; Andersen et al. 2018; Gordeychik et al. 2018; Ruth et al. 2018; Mutch et al. 2019; Devoir et al. 2021). Fewer still have modeled diffusion in multiple minerals from the same eruption (e.g., Chamberlain et al. 2014; Singer et al. 2016; Cooper et al. 2017; Fabbro et al. 2017; Flaherty et al. 2018; Shamloo and Till 2019; Magee et al. 2020). Generally, diffusion timescales calculated from a single element-mineral pair are extrapolated to the entire magmatic system, the assumption being that zonation present in one mineral represents the same events as zones that are similarly sequenced in another mineral from the same lava. For example, the most rim-ward zones in two types of minerals from the same lava might be expected to represent the same event when both minerals are in equilibrium with the melt. However, this hypothesis requires further investigation, which we and some other workers (e.g., Mutch et al. 2021) have undertaken.

In this work, we examine clinopyroxene from Yellowstone Caldera's Scaup Lake rhyolite. We compare its diffusive timescales to those of sanidine from the same lava flow, a mineral whose crystallization interval is believed to overlap that of the clinopyroxene (Brugman and Till 2019 and references therein). In this study we are interested in whether Scaup Lake clinopyroxene and sanidine record the same magmatic events, with the larger aim of addressing the similarities and differences of the pre-eruptive records of different minerals within the same lava flow.

We also examine the difference between chemical zonation that results *only* from diffusion, and chemical zonation that results from both mineral growth while magma body chemistry is changing *and subsequent* diffusion (hereafter referred to as "growth-then-diffusion"). It is important to model each case appropriately, depending on whether crystal growth and delivery of nutrient elements to the growth surface are thought to occur at similar rates over the relevant temperature range or if one process is faster than the other (Zhang 2008). In cases where delivery of elements to the growth surface (diffusion in the melt) is the dominant (i.e., faster) process, the final analyzed chemical profile is



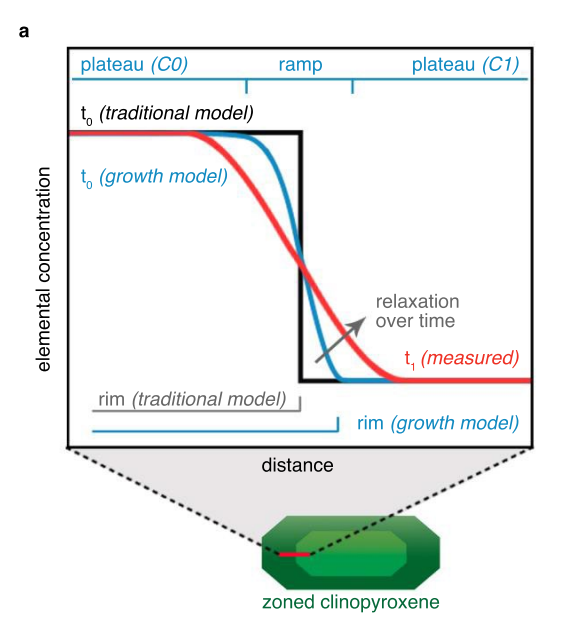
However, this method results in overestimated timescales if the Fe-Mg profiles are growth-dominated. If crystal growth occurs over comparable, or shorter, timescales than element diffusion in the melt, magma mixing, and melt composition evolution, the initial chemical profile prior to diffusive relaxation cannot be assumed to be a step function. This scenario requires an independent assessment of the initial chemical profile shape. To that end, timescales can be modeled utilizing two elements with vastly different diffusivities: a slower-diffusing element may be used to assess the initial profile shape, and a faster-diffusing element may be employed to assess the elapsed time since crystal rim growth (e.g., Costa et al. 2003, 2008; Milman-Barris et al. 2008; Till et al. 2015; Mutch et al. 2019). As suggested by recent studies (e.g., Till et al. 2015; Shamloo and Till 2019; Mutch et al. 2019), this approach is likely necessary for crystal-rich and/or high-silica magmatic systems where magma mixing is typically sluggish and in competition with crystal growth and diffusion rates.

Thus, in addition to comparing timescales from multiple mineral populations, we also develop a method using multiple elements from the same mineral to calculate diffusion timescales when the effects of both crystal growth and then diffusion must be considered. Recent studies have made strides to improve modeling methods and error reporting for diffusion chronometry (e.g., Gualda et al. 2012; Allan et al. 2013; Gualda and Sutton 2016; Cooper et al. 2017; Jollands 2020; Couperthwaite et al. 2021; Mutch et al. 2021) and here we also aim to further these efforts. We discuss and report error and urge the diffusion chronometry community to reevaluate the common practice of reporting a single diffusion timescale value as a precise chronometer.

# **Geologic setting and samples**

Yellowstone Caldera in NW Wyoming (Fig. 2a) is the youngest expression of the Yellowstone-Snake River Plain hotspot track which trends NE across the northwestern USA from its first apparent eruptive center in SE Oregon (ca. 16 Ma). The current caldera is the result of three major explosive rhyolitic eruptions that formed the Huckleberry Ridge Tuff at 2.09 Ma, the Mesa Falls Tuff at 1.30 Ma, and the Lava Creek Tuff at 0.63 Ma (Rivera et al. 2014, 2016; Matthews et al. 2015). Although these are among the largest explosive eruptions on Earth (with erupted volumes of approximately 2500, 280, and 1000 km³, respectively; Christiansen 2001), Yellowstone more commonly generates effusive rhyolitic eruptions. Yellowstone has produced more





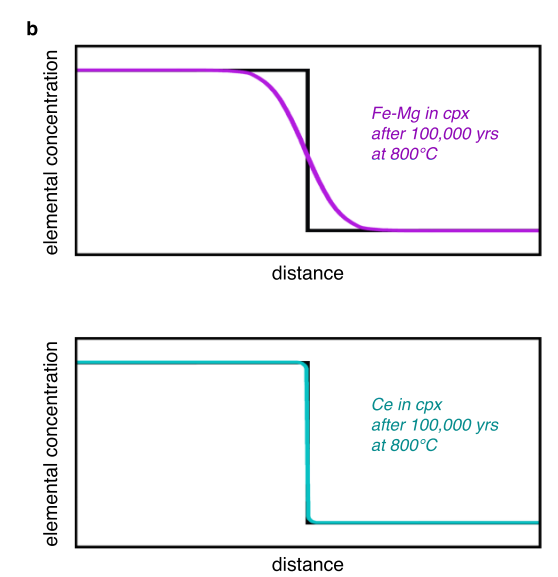


**Fig. 1** a Diffusive relaxation of trace element intracrystalline zoning in clinopyroxene. The black line (labeled "traditional model") shows the step function that is often used as the initial condition for diffusion modeling. In this work, the Ce concentration measured in clinopyroxene was used as a proxy to the growth-then-diffusion initial condition (blue line labeled "growth model"). This initial condition was used as a starting point for modeling diffusive relaxation of FeMg. An illustration of the present-day concentration of Fe measured in clinopyroxene is represented by the red line (labeled "measured").

**b** Comparison of synthetically-generated elemental concentration profiles for two elements that diffuse at different rates. Both Fe–Mg interdiffusion and Ce diffusion are modeled in clinopyroxene at 800 °C with a traditional step function initial condition (Van Orman et al. 2001; Dimanov and Wiedenbeck 2006). After the same amount of time, the profile of the faster diffusing Fe–Mg has considerably relaxed, but the profile of the slower diffusing Ce is nearly indistinguishable from the black step function initial condition

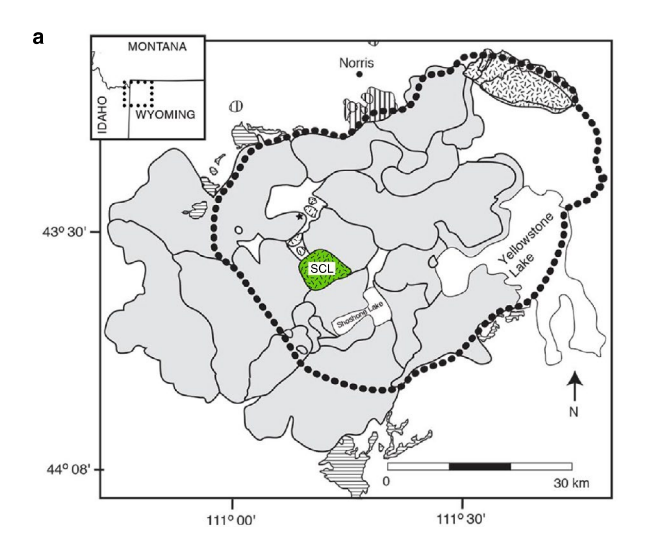
than 20 detectable flows since the last caldera-forming eruption (Fig. 2b), and future activity is likely to be effusive as well (e.g., Christiansen et al. 2007; Watts et al. 2012; Girard and Stix 2012; Stelten et al. 2015; Till et al. 2019). These effusive lavas are not negligible; the cumulative measurable volume of post-caldera lavas is > 350 km<sup>3</sup> with some individual units having erupted volumes > 50 km<sup>3</sup> (Christiansen et al. 2007).

The most recent post-caldera effusive eruptions can be divided into three groups: the early Upper Basin Member (UBM) rhyolites that erupted > 480 ka; the late UBM rhyolites that erupted ~ 260 ka; and the Central Plateau Member (CPM) rhyolites that erupted ~ 170–70 ka (Fig. 2b) (Till et al. 2019 and references therein). Exposed just south of the Mallard Lake resurgent dome, the ca. 262 ka (Christiansen et al. 2007) late UBM Scaup Lake rhyolite (SCL) eruption is significant because it marked the geochemical transition to the most recent CPM volcanic cycle at Yellowstone Caldera (Fig. 2b) (Vazquez et al. 2009; Till et al. 2019). This eruption, which occurred after a  $\sim$  220 kyr gap in the igneous record, emplaced 2–3 km<sup>3</sup> of glassy rhyolitic lava with 12-15 vol% phenocrysts, consisting of sanidine (40%), plagioclase (30%), quartz (20%), pyroxenes (7%), and Fe-Ti oxides (3%) (Till et al. 2019) (see Table 1 for bulk composition). Zircon crystallization ages for SCL are quite young, with only a few crystal cores dating to earlier than 500 ka, suggesting that magmatic conditions before SCL's eruption were hot enough to dissolve essentially all leftover zircons from early UBM magmas, or that the late UBM eruptions represent entirely different magma bodies that evolved exclusively after the earlier eruptions (Till et al. 2019). There is a progressive compositional and isotopic evolution from SCL through the subsequent CPM sequence, suggesting a linked petrological history marked by infusions of melted crust (Vazquez et al. 2009; Girard and Stix 2009, 2010; Watts et al. 2012; Loewen and Bindeman 2015; Stelten et al. 2017; Till et al. 2019). Previous diffusion chronometry on SCL sanidine indicates the timescale between the system's last chemical perturbation and eruption could be as short as a few decades or a few months (Till et al. 2015).

#### Scaup Lake clinopyroxene

Fe-rich clinopyroxene (cpx) is the most abundant mafic phenocryst in Yellowstone Plateau rhyolites (Christiansen 2001). SCL cpx are euhedral, isolated, and commonly ~0.5 mm, with some phenocrysts > 2 mm. Examination of SCL cpx





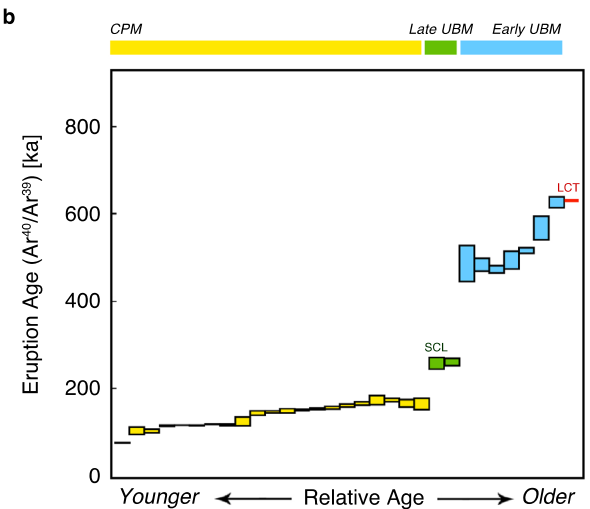


**Fig. 2** a Location of the Scaup Lake (SCL) rhyolite flow (green) in Yellowstone Caldera (present-day extent marked with dotted line). Patterned regions denote pre-caldera rhyolites (horizontal lines), extra-caldera rhyolites (vertical lines), and Upper Basin Member (UBM) rhyolites (hatched). Subsequent Central Plateau Member (CPM) rhyolites in gray. After Till et al. (2019) Fig. 2, and originally based on the geologic mapping of Christiansen (2001) **b** Diagram showing the sequence of eruptions at Yellowstone since the last caldera-forming eruption, the Lava Creek Tuff (LCT, red, 630 ka). SCL is labeled in green and erupted ca. 262 ka. Box height indicates 2 sigma error in Ar<sup>40</sup>/Ar.<sup>39</sup> eruption age. After Till et al. (2019) Fig. 1. Data: Christiansen et al. 2007; Matthews et al. 2015; Stelten et al. 2015, 2018; Till et al. 2019

via backscattered electron imaging (BSE) shows exsolution lamellae and Fe–Mg reverse-zoned crystals with fine outer zones, e.g.,  $<40 \mu m$  wide (Fig. 3).

Cpx is an appealing, although perhaps unexpected, choice to compare to preexisting diffusion timescale estimates from SCL sanidine (e.g., that of Till et al. 2015). Recent studies have articulated a phenomenon known to experimental petrologists who conduct high-silica phase equilibria studies:

cpx, while considered to be a high temperature mafic mineral, is not limited to high temperatures in rhyolitic systems (Almeev et al. 2012; Gardner et al. 2014; Iacovino et al. 2015; Bolte et al. 2015; Befus and Gardner 2016; Brugman and Till 2019). Instead, experiments confirm that cpx is stable at or near the solidus to temperatures below 700 °C in rhyolitic magmas (Almeev et al. 2012; Gardner et al. 2014; Iacovino et al. 2015; Bolte et al. 2015; Befus and Gardner 2016). Indeed, some cpx are included in quartz and sanidine, indicating that cpx crystallization happens earlier than, or at the same time as, that of these felsic minerals. This is consistent with experimental work done on Yellowstone CPM phase relationships, in which cpx was found to crystallize after sanidine and only ~ 20 °C before quartz (Befus and Gardner 2016). This overlap in crystallization intervals allows for the possibility of correlating the recorded timescales between these minerals.

# **Analytical methods**

# Sample preparation

In situ electron probe micro-analyzer (EPMA) analyses (Brugman et al. 2022, Online Resource 1) were conducted on carbon-coated SCL rhyolite thin sections. For laser ablation inductively coupled plasma mass spectrometry (LA-ICP-MS) and secondary ion mass spectrometry (SIMS) analyses, single cpx crystals with intact faces were hand-picked under stereo microscope from a < 1 mm fraction of separates from the SCL lava flow basal vitrophyre. This sample, YCV-08, was collected under National Park Service research permit YELL-2012-SCI-5920 and is the same sample used in the Till et al. (2015) study. The single crystals were mounted in epoxy with c-axes parallel to the surface of the mount. Cpx for NanoSIMS analysis were prepared in the same way with the exception that the crystals were mounted in epoxy wells drilled into 1" aluminum rounds to reduce outgassing under high vacuum. The crystal separate mounts were polished to expose central cross sections of the cpx using an auto-polisher and diamond suspension pastes to 0.25 µm, then were gold coated.

## **LA-ICP-MS and EPMA**

Cpx elemental abundances were measured at the Group 18 laboratory at Arizona State University (ASU) using a Thermo Scientific iCAP Qc quadrupole LA-ICP-MS with a Photon Machines Analyte G2 ArF Excimer 193 nm UV laser with a HelEx II ablation cell. Helium gas flow to the HelEx II ablation cell was 0.2 LPM (L/min) to the chamber and 0.4 LPM to the cup, and was mixed with 0.98 LPM of Ar before



**Table 1** Scaup Lake whole rock and clinopyroxene compositions

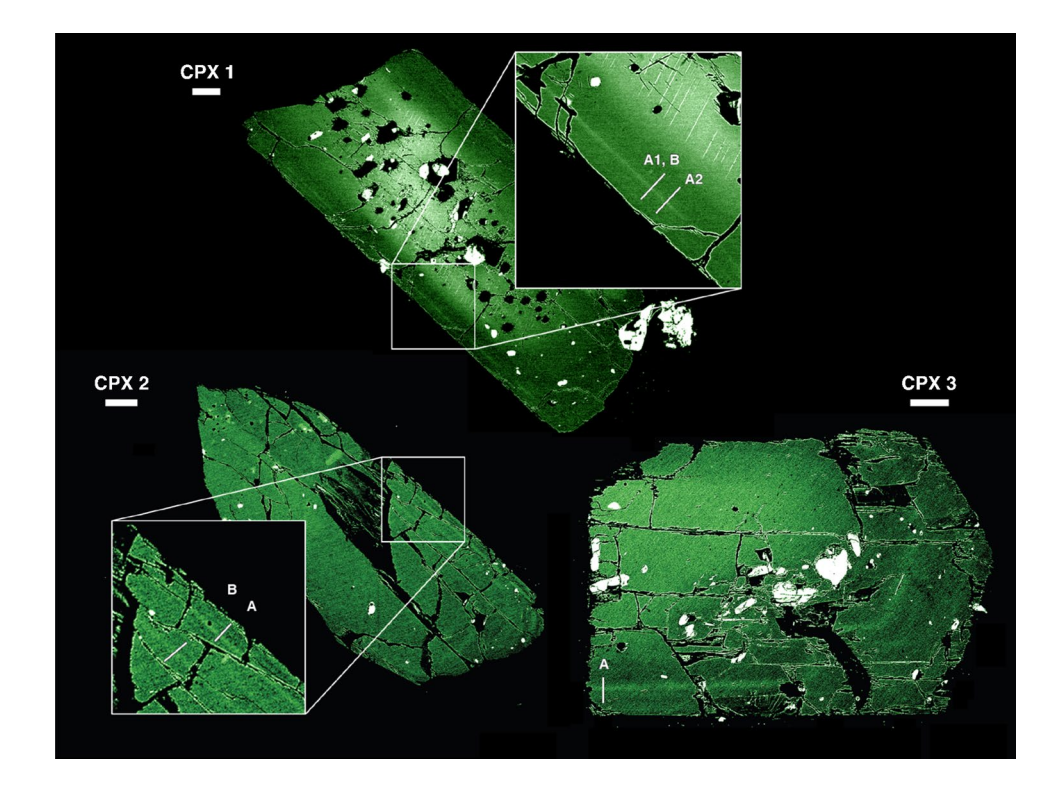
	Whole Rock*		Clinopyroxene**			
	wt%	r.s.d. <sup>†</sup>	Rims		Cores	
			wt%	s.d	wt%	s.d
SiO <sub>2</sub>	73.26	0.19	51.71	0.31	51.00	0.58
$TiO_2$	0.259	0.25	0.18	0.02	0.20	0.04
$Al_2O_3$	12.51	0.05	0.66	0.08	0.62	0.11
$Cr_2O_3$			0.00	0.01	0.00	0.01
FeO <sup>tot</sup>	1.69	0.22	15.36	0.47	18.22	1.81
MnO	0.043	1.84	0.75	0.05	0.92	0.10
MgO	0.23	10.83	11.10	0.22	9.72	0.87
CaO	0.84	0.00	19.92	0.26	19.01	0.49
Na <sub>2</sub> O	3.30	0.20	0.31	0.02	0.30	0.02
$K_2O$	5.18	0.13	0.03	0.02	0.01	0.01
$P_2O_5$	0.036	2.66				
Mg#			56.31	1.10	48.77	4.70

Mg# is unitless. Italicized values indicate standard deviation

entering the torch of the ICP-MS. Spots were 35–50  $\mu$ m and laser on duration was 20 s. The fluence at the sample surface was ~7.56 J/cm<sup>2</sup>.

Measurements of cpx and glass (Brugman et al. 2022, Online Resource 1) for geothermometry calculations were performed on the JXA-8530F EPMA at ASU's Eyring Materials Center using an accelerating voltage of 15 kV and beam current of 15 nA. Count times were 40 s for Mg and Ca; 30 s for Si, Ti, Al, Cr, Fe, and Mn; and 20 s for Na and K. Spot sizes were 1  $\mu$ m for crystals and 10  $\mu$ m for glass. The EPMA was also used to identify intracrystal-line zone boundaries of interest via BSE images.

Fig. 3 False color backscattered electron (BSE) images of Scaup Lake clinopyroxene showing the locations of the NanoSIMS profiles. All profiles were measured from core to rim. Crystals are reverse-zoned; lighter areas in the clinopyroxene correlate with higher Fe content (brightness is not calibrated across images). Scale bars are 100 µm





<sup>\*</sup>XRF data; from Girard and Stix (2009)

<sup>\*\*</sup>EPMA data; rims n = 122, cores n = 60

 $<sup>\</sup>dot{\tau}$  Relative standard deviation of three standard analyses from the cited manuscript's Supplementary Data

# Crystal selection for NanoSIMS analyses and diffusion modeling

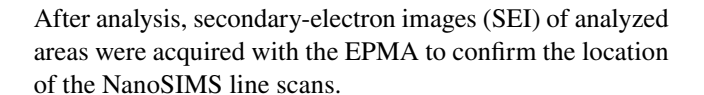
Overall, we observed zoning in ~34% of the BSE images of cpx crystals we collected for reconnaissance. Of the crystals with zoning in BSE images, ~95% had a broad inner zone (see Fig. 3), ~24% had what we call medium oscillatory zones (between the rim of the crystal and the broad inner zone), and ~10% had fine rim zones. However, this ~10% with fine rim zones is not a reflection of the true proportion of these crystals present in the lava. Many of the cpx crystals mounted for BSE imaging and further study were fragments that lost the euhedral rims apparent in thin section during the rock crushing and mineral separation process. We limited our NanoSIMS data collection to crystals or portions of crystals that included euhedral rims and thus the fine outer zones.

 $\sim 25\%$  of the crystals we examined contain exsolution lamellae; however, this is not a consistent feature of crystals with fine outer rim zones. Additionally, because the fine outer zones are found in the outer  $\sim 100$  µm of the crystals, they indicate very late events in the crystal's history, likely after any cooling that caused exsolution.

#### SIMS and NanoSIMS

Intracrystalline zone boundary profiles of the elements of interest were measured with the Cameca Ametek IMS 6f SIMS at ASU's National Science Foundation (NSF) Multi-User Facility. SIMS profiles were measured with an accelerating voltage of -12.5 kV and a primary beam intensity of 10 nA of  $O^-$  gated to 4 µm, with  $\leq 8$ -µm step size between analysis points. Count times per cycle were 1 s for  $^{30}$ Si,  $^{54}$ Fe, and  $^{26}$  Mg and 5 s for  $^{140}$ Ce.

ASU's NSF Multi-User Facility Cameca Ametek Nano-SIMS 50L was used to complete line scans across SCL cpx intracrystalline boundaries for diffusion chronometry modeling. Single rim profiles were measured for cpx in "beam control" mode where the beam was monitored and moved to consecutive analysis locations on a predefined line. Consecutive rim profiles were measured to provide an extra check when confirming modeling results. In some cases, duplicate profiles were measured of the same zone boundary, also as an additional check. All line scans were measured perpendicular to the c-axis. A total of 60 line scans, each including measurements of Mg, Si, Fe, Ce, and Dy, were measured in 16 cpx grains with an accelerating voltage of 16 keV and a primary beam intensity of 50 pA of O-. Linescans were 37–77 µm long with 0.2–1 µm spacing between analysis points taken with a beam size of 500-750 nm. These represent some of the first cpx trace element analyses conducted via NanoSIMS, and so a variety of settings were explored including the variable use of apertures D1-1, D1-2, or D1-3.



# Geothermometry

Temperature was calculated using a cpx-liquid geother-mometer specifically calibrated for the high-Fe, low-Al cpx found in high-silica igneous systems (Brugman and Till 2019). SCL cpx rims yielded a temperature of  $800 \pm 20$  °C. Isothermal diffusion was assumed due to the portion of the lava flow sampled (the quenched base) and the low variance of Mg# for the cpx rims (average:  $56.31 \pm 1.10$ ; Table 1).

# Diffusion chronometry modeling

#### A need for a growth-then-diffusion initial condition

Preliminary analyses via SIMS revealed elemental profiles with quantifiable variation across intracrystalline zone boundaries, but of inadequate spatial resolution for diffusion chronometry modeling. The zone boundaries in the cpx were quite narrow (only a few 10s of micrometers wide) compared to the SIMS' spatial resolution. To mitigate convolution, at least three analysis points must be measured across the profile "ramp", the area of the elemental concentration profile showing transition from one concentration to another (Fig. 1a). Therefore, analyses with higher spatial resolution were required to sufficiently quantify concentration gradients for diffusion modeling. The NanoSIMS was determined to be the best tool to collect profiles for modeling diffusion in SCL cpx. Out of 60 NanoSIMS line scans, the six segments selected for diffusion chronometry modeling exhibited the clearest element concentration profile plateaus and ramps in locations corresponding to BSE zoning. Profiles were discarded for various reasons including a too low signal-tonoise ratio, edge effect interference, and indistinct plateaus. Si-normalized Fe and Ce abundances used for diffusion modeling typically varied by 85% and 82%, respectively.

Calculations using our NanoSIMS data and a traditional diffusion modeling approach utilizing an analytical solution to the diffusion equation reinforced the hypothesis that the initial condition in SCL cpx cannot be approximated by a step function. Here, concentration profiles of different elements collected simultaneously in multi-collection mode on the Nano-SIMS appear to be approximately the same length (Online Resource 2), which is not possible for elements that differ in diffusive rate by several hundred times (Van Orman et al. 2001; Costa and Morgan 2011). After the same amount of time, faster-diffusing elements should have longer ramps than those of slower-diffusing elements. For example, Fig. 1b shows sample diffusion profiles for elements that diffuse at different



rates, modeled at the same temperature (800 °C) in cpx, and using a step function initial condition. After 100,000 years, the ramp of an Fe-Mg profile would be ~ 100 μm wide, but a Ce profile would be < 2 µm wide. In practice, this means that if elements begin diffusing from a step function initial condition, different elements' concentration profiles across the same zone boundary should be different widths and should give the same diffusive timescale. However, the measured profiles from different elements were of similar width and yielded timescales that deviated by at least one, and often multiple, orders of magnitude (e.g., an Fe profile time of 4 kyr versus a Ce profile time from the same line scan of > 11 Myr). Together, the indistinguishable length of the profiles and the large variance in traditional diffusion chronometry timescales strongly indicate that SCL elemental concentration profiles across intracrystalline zone boundaries recorded growth-then-diffusion.

#### **Modeling methods**

Diffusion modeling is based on Fick's second law:

$$\frac{\partial C}{\partial t} = D\left(\frac{\partial^2 C}{\partial x^2}\right) \tag{1}$$

where  $\frac{\partial C}{\partial t}$  is the position-independent change in elemental concentration over time, D is the diffusion coefficient (Eq. 2), and D is independent of C (concentration) or x (position). An element's diffusion coefficient, D, is calculated by:

$$D = D_0 e^{-\frac{E}{RT}} \tag{2}$$

where  $D_0$  is a preexponential factor, E is the activation energy, R is the gas constant, and T is the temperature at which diffusion occurs (see "Diffusion coefficients used in modeling" for details). D also depends on the magma body temperature, pressure,  $fO_2$ , and the mineral type, element, and crystallographic direction of diffusion. Because these cpx crystals are from the same lava and due to the care taken to prepare samples for analysis, we assume uniform pressure,  $fO_2$ , and crystallographic direction of diffusion (perpendicular to the c-axis) and therefore use Eq. 2 to calculate D for all models.

We modeled one-dimensional position- and concentrationindependent diffusion in SCL cpx using both the diffusion only (step function) and growth-then-diffusion initial conditions. In all cases, the chemical profiles are first fit using the analytical solution to the diffusion equation assuming a planar, semiinfinite source:

$$C = C1 + \left(\frac{C0 - C1}{2}\right) * Erfc\left(\frac{x}{2\sqrt{Dt}}\right)$$
 (3)

where C0 and C1 represent the elemental concentrations of a given element at the left- and right-hand plateaus,

respectively (Fig. 1a), D is the diffusion coefficient, t is elapsed time, and Erfc is the complimentary error function. This approach was employed in a Monte Carlo model to calculate timescales from a single element-mineral pair from a step function initial condition. For the growth-then-diffusion case, where we do not assume a step function initial condition, we utilized a Monte Carlo finite differences forward model. The best times reported are median, not mean values (see Online Resource 5 for further discussion) and we propagated error for  $D_0$ , E, and T, accounting for the covariance of  $D_0$  and E (Online Resources 3 and 4) as suggested by others in the diffusion community (e.g., Mutch et al. 2021; see "Sources of Error" for further discussion).

Our growth-then-diffusion initial condition proxy method differs from the binary-element diffusion modeling (BEDM) method of Morgan and Blake (2006). That study cleverly avoids the problem of determining the initial condition by using forward modeling of a slower diffusing trace element to match the absolute amount of diffusion of a faster diffusing trace element to determine magmatic residence times (Morgan and Blake 2006). Here however, we use the *shape* of the slower diffusing, similarly partitioning element as a proxy to the faster diffusing element's initial condition.

Suitable profiles for our growth-then-diffusion initial condition proxy method were selected according to the following criteria: adequate plateaus; inclusion of at least three data points on the ramp, which is required to mitigate convolution; and the ability to fit a curve on a short enough timescale to be reasonable for SCL (e.g., less than the difference in time between the last caldera-forming eruption and the eruption of SCL) (Morgan and Blake 2006). Only two profiles were modeled using our growth-then-diffusion initial condition proxy method because even with the high spatial resolution of the NanoSIMS, most SCL cpx intracrystalline zone boundary profiles were too narrow to yield enough data points to satisfy these conditions. We look forward to further refinement of NanoSIMS settings and techniques as well as future analytical instruments that will be able to better resolve these nanoscale features.

Errors were calculated for both diffusion modeling approaches. For both methods, the reported best-fit time interval represents the time interval in our model search that produced the lowest root mean square (RMS) misfit between the measured and modeled profiles. The misfit relationships we obtain are bounded by time = zero and are limited by the shape of the elemental profile itself, and so uncertainty bounds are reported as asymmetric confidence intervals (see further discussion in "Error"). 95% confidence intervals for the timescales were determined by the results of the Monte Carlo modeling approach, which produced a distribution of best fit model times.



# Element chosen as a proxy to the Fe initial condition

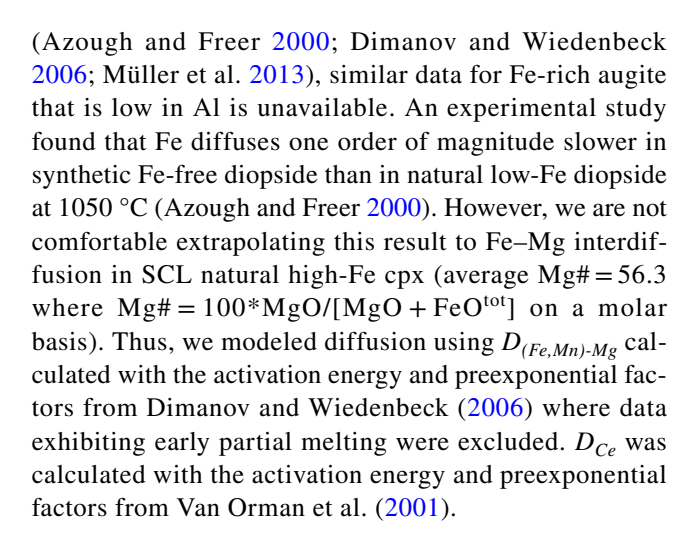
We used Ce to determine the initial condition when modeling the interdiffusion of Fe–Mg in cpx in our finite element diffusion approach. The coupled diffusion of Fe and Mg are usually used for diffusion chronometry modeling in cpx. So, we investigated a variety of possible elements in cpx with diffusivities slower than Fe–Mg. We focused on cations with unfavorable charges or large radii. LA-ICP-MS analyses of SCL cpx revealed that overall, they contained ~ 175 ppm of Ce, such that it should be present in sufficient quantities to yield a measurable concentration profile.

For a Ce elemental concentration profile to be used as a proxy to the Fe–Mg initial condition, it must partition into cpx in a similar manner to that of Fe and Mg. Fe and Mg are highly compatible elements with partition coefficients ( $K_d$ ) up to 13.1 for Fe and 20.4 for Mg in cpx found in rhyolite (Sisson 1991). Therefore, to use Ce in our modeling, this element must also have  $K_d > 1$  in cpx. Indeed, Ce has been shown to partition compatibly into high-Fe cpx with  $K_d$  ranging from 2.5 to 20.9 (Mahood and Hildreth 1983; Sisson 1991).

Published diffusion coefficients for rare earth elements (REE) show that Ce can diffuse > 700 times slower in cpx than Fe and Mg (Van Orman et al. 2001; Costa and Morgan 2011). That diffusion study (Van Orman et al. 2001) was conducted on diopside that presumably contained trivalent Ce. We deem the comparison of this Ce<sup>3+</sup> diffusion coefficient to that of Fe–Mg to be appropriate, because a change in Ce oxidation state from Ce<sup>3+</sup> to Ce<sup>4+</sup> would require a compensating M1 site vacancy (an increase in this vacancy would facilitate diffusion) or a substitution of Al<sup>3+</sup>. As SCL cpx has a very low Al<sub>2</sub>O<sub>3</sub> content (~0.6 wt%, Table 1) it seems unlikely that quadrivalent Ce is present in sufficient quantities to affect Ce's diffusivity. Therefore, Ce is indeed likely to diffuse several hundred times slower in cpx than Fe–Mg.

## Diffusion coefficients used in modeling

Diffusion studies of cpx in rhyolitic systems are hampered by a lack of experimental data for the low-Al, high-Fe cpx common to high-silica systems (Brugman and Till 2019). Higher Al contents must be charge balanced by  $Fe^{3+}$  and a vacancy ( $Fe^{2+} = Al^{3+} + Fe^{3+} + [\ ]$ ), resulting in more point defects in the crystal lattice. This allows for faster diffusion to occur in a high-Al cpx than in a low-Al cpx with an otherwise comparable composition. Whether Fe–Mg interdiffusion occurs at a slower rate for the low-Al, high-Fe cpx crystallized in high-silica systems is as yet untested. Although experimental Fe and Fe–Mg diffusion studies have been conducted to determine E,  $D_0$ , and therefore D for cpx at temperatures of 800–1200 °C



# **Crystal growth rates**

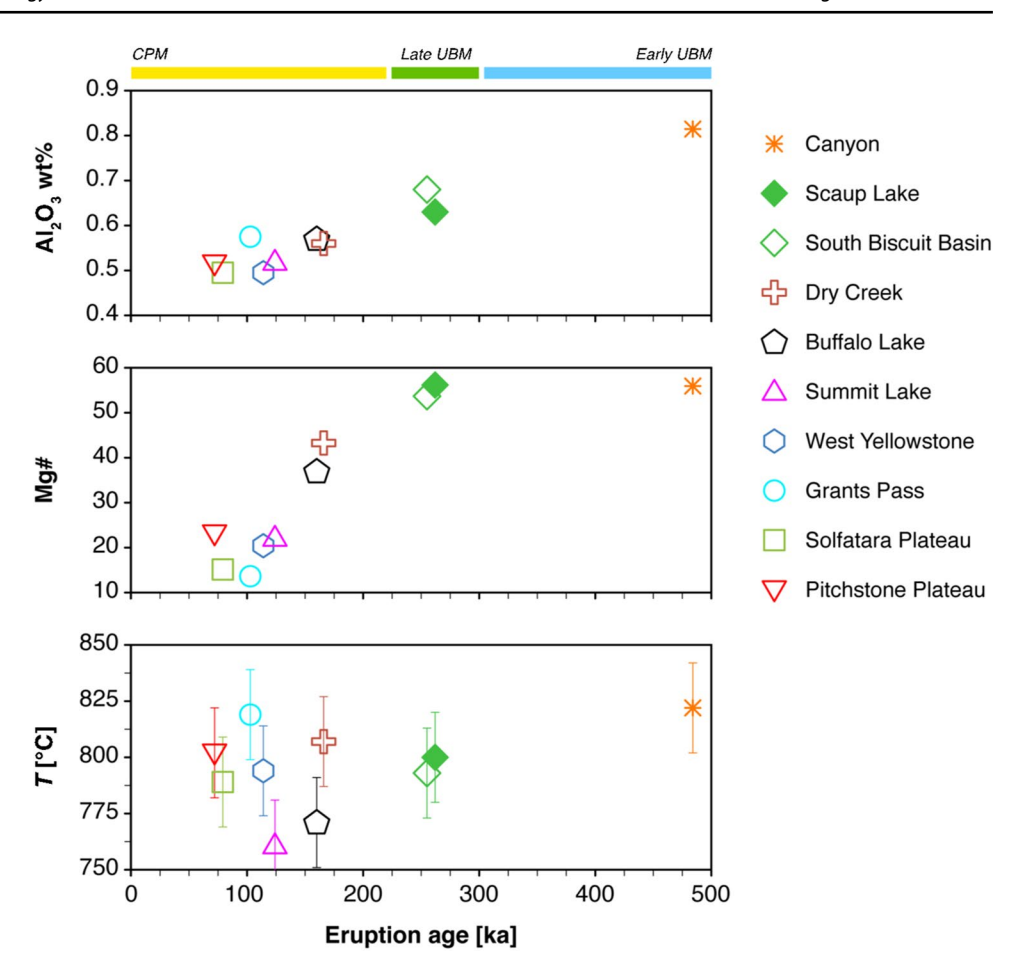
The usefulness of diffusion chronometry in a mineral depends on the contrast between the rate of chemical change an individual crystal experiences, versus the crystal growth rate, i.e., how fast information can be recorded in the crystal rim. Because we assume the Fe and Ce initial profile shapes are the same, we therefore assume that although the surrounding melt's composition changed during crystal growth, there was no relative change in the elements' partition coefficients, i.e., no relative change in the concentration of these two elements to each other in the cpx. This assumption also implies that no boundary layer formed around the crystal, a phenomenon that is generally a result of crystal growth that outpaces the ability of the surrounding melt to diffuse elements to the growing crystal edge (diffusion controlled growth). We deem these to be acceptable assumptions due to the low Al content of SCL cpx.

As mentioned above, SCL cpx have extremely low  $Al_2O_3$  (~0.6 wt%, Table 1, Fig. 4), as do many high-silica magmatic system cpx (Brugman and Till 2019). In fact, the younger the Yellowstone post-caldera lava, the more FeO rich and  $Al_2O_3$  poor the cpx becomes, a trend that does not appear to correlate with cpx crystallization temperature (Fig. 4). Because low Al content in these cpx is likely a result of their low Ca content (the resulting charge imbalance with O3 oxygen requires more Si to occupy tetrahedral sites to compensate) (Salviulo et al. 2000), it is likely that low bulk CaO content (<0.5 wt% for CPM lavas) (Girard and Stix 2010) as well as the crystallization of plagioclase (30% of SCL phenocrysts) (Till et al. 2019) indirectly caused this depletion of Al in cpx.

Low Al content in cpx could also imply slow crystal growth. Low Al in basaltic cpx has been correlated to slow cooling rates, as well as to the more slowly-grown crystals found in the warm interiors of lava flows (Mollo et al. 2010). In that study (Mollo et al. 2010), high Al in cpx was



Fig. 4 Al<sub>2</sub>O<sub>3</sub> wt%, Mg#, and clinopyroxene-liquid temperature (Brugman and Till 2019) of Yellowstone clinopyroxene versus <sup>40</sup>Ar/<sup>39</sup>Ar eruption date in kyr before present (ka). The younger the post-caldera lava, the more FeO rich and Al<sub>2</sub>O<sub>3</sub> poor the clinopyroxene becomes, a trend that does not appear to correlate with clinopyroxene crystallization temperature. Member names as suggested by Till et al. (2019). Data: Christiansen 2001; Vazquez et al. 2009; Girard and Stix 2010; Pritchard and Larson 2012; Befus and Gardner 2016



associated with a crystal growth regime in which less compatible elements were incorporated due to the formation of a boundary layer around the growing crystal. This suggests a congruent possibility for high-silica cpx before eruption: the low Al in Yellowstone post-caldera cpx could also signal slower growth. Although this hypothesis is not confirmed, the SCL cpx themselves do support it. For example, SCL cpx are low in Al (although this could have other causes as described above), large, euhedral, and free of features such as sector zoning that would indicate fast growth. The slower-growth possibility is interesting because slow, constant growth could allow a crystal to capture a higher resolution record of chemical changes in the melt. However, this same information fidelity presents problems when attempting traditional diffusion modeling (see "Diffusion chronometry methods").

# Diffusion chronometry timescales and recorded events

Figure 5a summarizes the diffusion timescales obtained from six rim profiles from three SCL cpx crystals. The x-axis shows time in years before the eruption of SCL, with that eruption occurring at the far left. Crystals are designated

CPX1, CPX2, and CPX3. NanoSIMS profiles are named in order of occurrence from rim to core, e.g., CPX2 zone A was measured closer to the rim than CPX2 zone B. Profiles CPX1 zone A1 and CPX1 zone A2 are two measurements of the same zone, at different locations on the crystal. Timescales are shown with matching-colored 95% confidence intervals (note that the confidence intervals in panel 2 are essentially identical, so the two colors are difficult to discern).

Panels in Fig. 5 are grouped according to the modeling method used. Panels 1–3 show timescales modeled using a traditional step function initial condition, grouped by timescale. Panels 4–5 show timescales modeled using the growth-then-diffusion proxy initial condition. Profile colors are consistent across these two methods. For example, profile CPX2 zone A was modeled using both methods, and appears in red in both panels 2 and 4. Panels 6–8 show the discrete events binned from the results shown in panels 1–5 (see more below) and panel 9 shows timescales from a previous study on SCL sanidine (Till et al. 2015).

Cpx profiles CPX2 zone A (red) and CPX3 zone A (blue) were modeled using the growth-then-diffusion initial condition proxy method with all D error contributors (E,  $D_0$ , and T) propagated. This method gave timescales of  $1000^{+1400}_{-500}$ 



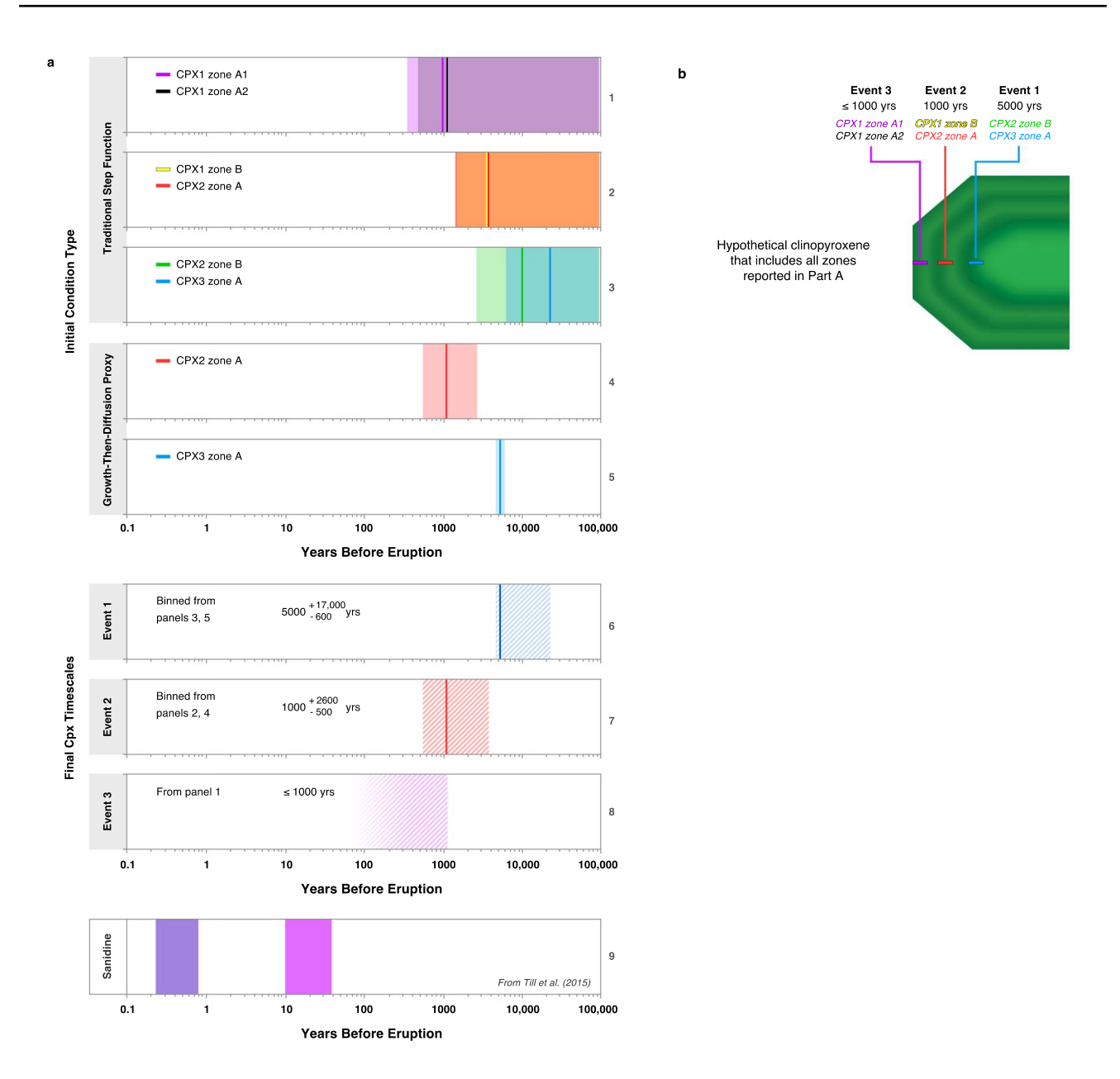


Fig. 5 a Diffusion chronometry modeling results for Scaup Lake cpx rims using a traditional step function (panels 1–3) or growth-then-diffusion (panels 4–5) initial condition. Colored solid vertical lines indicate best fit times (maximum possible times for panels 1–3, actual times for panels 4–5) and colored shaded areas show 95% confidence intervals. The red profiles in panels 2 and 4 and the blue profiles in panels 3 and 5 are the same NanoSIMS profiles, respectively, modeled using each of the two types of initial conditions. Note that there is not a predictable relationship between the calculated timescales. For the red profiles (CPX2 zone A), the calculated timescales are within a few thousand years of each other. However, for the blue profiles (CPX3 zone A), the two timescales differ by more than an order of magnitude. Cool colored profiles (panels 3, 5) and warm colored

and  $5000^{+800}_{-600}$  years before eruption (95% confidence, Fig. 5 panels 4–5). The same profiles modeled using the traditional step function initial condition gave maximum timescales

profiles (panels 2, 4) were binned together to calculate the final time-scales in panels 6 and 7, respectively. Panel 8 shows a maximum timescale for the event recorded by the profiles in panel 1 (see "Diffusion modeling results" for a discussion of why this timescale bin cannot be combined with Event 2). Panel 9 shows timescales from sanidine rims as reported by Till et al. (2015). Although all timescales in this figure are from the crystals' outermost rims, the clinopyroxene do not yield timescales explicitly on the order of months to tens of years, nor do the sanidine yield timescales > 100 years. **b** Cartoon illustrating the order of zones that produce the timescales reported in Part A (in years before eruption of SCL), if a single crystal were to have recorded all three events

of  $3600^{+91,300}_{-2300}$  and  $22,400^{+70,000}_{-16,300}$ , respectively (95% confidence, Fig. 5 panels 2–3). Profiles that could not be modeled using the growth plus diffusion initial condition proxy were



modeled using the traditional step function initial condition (with propagated *T* error; Fig. 5 panels 1–3 in purple, black, yellow, and green).

Figure 5b illustrates the rim to core relative positioning of the modeled profiles. As expected, consecutive rim profiles (proceeding from rim to core) from the same crystal give older modeled times e.g., CPX1's rim-ward profile, zone A1 (Fig. 5 panel 1, purple) versus the older core-ward profile, CPX1 zone B (Fig. 5 panel 2, yellow) and CPX2's rim-ward profile, zone A (Fig. 5 panels 2 and 4, red) versus its older core-ward profile CPX2 zone B (Fig. 5 panel 3, green). We also see timescale agreements between outer zone boundaries measured in two different locations on the same crystal, e.g., CPX1 zone A1 and CPX1 zone A2 (Fig. 5 panel 1, purple and black, respectively). Also apparent are agreements between outer zone boundaries from different crystals, e.g., CPX2 zone A and CPX1 zone B (Fig. 5 panel 2, red and yellow, respectively) and CPX2 zone B and CPX3 zone A (Fig. 5 panel 3, green and blue, respectively).

Profiles were binned into three separate rim zone timescale populations which represent three discrete pre-eruptive events (Fig. 5 panels 6–8). To do this, we used the above constraints, as well as the maximum timescales calculated using the traditional step function initial condition. For example, Event 1 was binned from panels 3 and 5 because (1) the same profile was modeled in each panel (CPX3 zone A, blue); and (2) the two profiles shown in panel 3 are of a similar magnitude with overlapping 95% confidence intervals. The three bins represent separate events at  $5000^{+17,000}_{-600}$ years,  $1000^{+2600}_{-500}$  years, and a maximum of 1000 years before eruption (Fig. 5 panels 6-8; see "Recommendations for error reporting" for a discussion of how these uncertainty intervals were determined). The latter is reported as a maximum timescale because it is based on timescales calculated using a traditional step function only. Note that it is not possible to change these populations by combining timescales from, for example, panels 1 and 2, which were binned as Event 3 and Event 2, respectively (Fig. 5b). These bins cannot be combined because panel 1 includes a timescale derived from one zone boundary from crystal CPX1, and panel 2 includes a timescale from a different zone in the same crystal (see also Fig. 5b). Similarly, timescales from panels 2 and 3 cannot be combined into one bin because each includes a timescale from a separate zone boundary on crystal CPX2 (see also Fig. 5b).

Figure 5a illustrates the difference between the best time calculated using the growth-then-diffusion initial condition proxy (panels 4–5) versus the *maximum possible* time calculated using a step function initial condition for the same profiles (Panels 2–3, CPX2 zone A in red and CPX3 zone A in blue). Note that for the profile from CPX2 zone A, the maximum timescale (Fig. 5 panel 2, red line) aligns nicely with the upper end of the 95% confidence interval for the

growth-then-diffusion best time (Fig. 5 panel 4, red field). However, the maximum timescale should not be considered a shorthand for determining the error envelope for profiles that result from growth-then-diffusion, as there is no correlation between the maximum time and the upper boundary of the best time error envelope for the profile from CPX3 zone A (Fig. 5 panels 3 and 5, blue).

It is important to note that if the timescales calculated using the traditional step function initial condition were not presented as a probable maximum boundary on time, the proposed timeline of events for SCL could be erroneously shifted to far longer times than actuality. For example, if we reported the timescale for Event 1 based on the step function initial condition modeling (Fig. 5 panel 3), we might average these two timescales, giving a time for Event 1 of  $16,200_{-11,800}^{+77,400}$  years. This overshoots our best time from the growth-then-diffusion initial condition proxy method for Event 1 (5000 years, Fig. 5 panel 6) by over an order of magnitude. In this case, the low end of this averaged timescale's 95% confidence interval does just overlap with our best time from the growth-then-diffusion initial condition proxy method (panel 5). However, this is not the case for the 95% confidence interval for Event 2.

Because we are interested in comparing timescales from SCL cpx rims to timescales from other mineral rims, our reported best timescales were modeled by propagating all D error contributors  $(E, D_0, \text{ and } T)$  as discussed below.

#### **Error**

#### Sources of error

We used Monte Carlo simulations to account for and compare sources of error. Note that because we assume uniform pressure, fO<sub>2</sub>, and crystallographic direction of diffusion (perpendicular to the c-axis) for our samples, these are not included in our error calculations. Future workers will likely wish to account for these in their calculation of D. We also recognize that there is no experimental study on cpx that perfectly matches those found in SCL, and so a future study that characterizes the diffusivity of low-Al, high-Fe will likely shift our calculated timescales. In the meantime, we have used the best-fitting empirical data available (see "Diffusion coefficients used in modeling"). The first source of error is the selection of the physical geometry of the profile when using the analytical solution to the diffusion equation (Eq. 3). C0 and C1 (Fig. 1a) for each measured profile can be estimated by either (1) visually selecting a range of concentration values for which a horizonal line would make sense for a plateau; or (2) averaging the points along the purported plateau segment of the profile and then using the analytical error of the data collection method to create  $a \pm 1$ 



sigma range of concentration values. Our calculations show no significant difference in misfit between the two methods if the former is reasonably constrained (average difference of misfit =  $2.3 \times 10^{-6}$ ). Therefore, our Monte Carlo error estimation used a synthetic normal distribution of possible CO and CI values in a given range to fit profiles in the analytical solution model.

The second source of error is the set of variables used to calculate the diffusion coefficient (Eq. 2), which include temperature (T), activation energy (E), and the preexponential factor  $(D_0)$ . E and  $D_0$  are determined via an Arrhenius plot of diffusion experiment results; E is the slope of this plot and  $D_0$  is the y-intercept. Of course the most appropriate experimental calibration for the mineral type and composition must be used if any subsequent results are to be trusted (see "Diffusion coefficients used in modeling" for a discussion of how these were selected for this study). E and  $D_0$  are said to exhibit covariance because plots with steep (higher value) slopes have higher y-intercept values than plots with shallower (lower value) slopes (Mutch et al. 2021). Their associated error therefore also covaries, so this relationship must be accounted for during modeling, lest a high E be paired with a low  $D_0$  when randomly selecting values during the Monte Carlo.

If covariance is not considered, an artificially large range of possible Ds are calculated as illustrated in Fig. 6. In this example, although both D distributions capture similar median (peak) values, note that the curve with covariance (Fig. 6, green) is compact with a log-normal shape and a limited range of values, up to  $< 3.0 \times 10^{-23} \text{ m/s}^2$ . The distribution of Ds calculated without covariance (Fig. 6, red) has a higher peak (this results from the model producing a similar value many times) that might be deceptively appealing. But notice that the tail of the curve is very long, indicating that improbably high values for D have been produced, up to  $\sim 2.7 \times 10^{-22} \text{ m/s}^2$ , or more than one order of magnitude greater than the expected value of  $1.18 \times 10^{-23} \text{ m/s}^2$ . The 95% confidence interval for these Ds without covarying E and  $D_0$ 

is  $0.31-1.80\times10^{-23}$  m/s<sup>2</sup>. The 95% confidence interval for *D*s when accounting for covariance is  $1.16-1.37\times10^{-23}$  m/s<sup>2</sup>

The greatest source of error in diffusion chronometry is the error associated with the temperature at which modeling will be performed, or more precisely, the error associated with the mineral geothermometer used to calculate this temperature. The large influence of temperature on diffusive timescales is due to the Arrhenius relationship of T to D (Eq. 2) and reflects an exponential increase in diffusion rate as point defects in the crystal lattice increase with temperature; a  $\Delta T$  of just 50 °C can result in a change in time ( $\Delta t$ ) of approximately one order of magnitude (Fig. 7). In Fig. 8 we examine the effect of temperature on resulting timescales by modeling via our finite difference method and propagating only T error. Modeled misfit is shown with a color ramp, with black being the lowest misfit and therefore corresponding to the most desirable modeled time. Note that while there

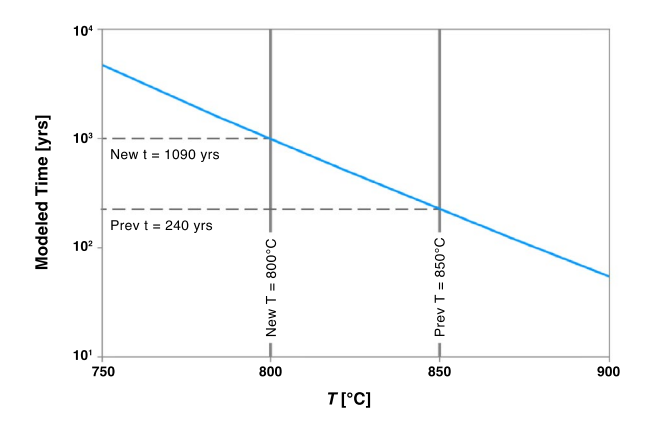


Fig. 7 The change in modeled diffusion timescale as a function of model temperature for a Scaup Lake cpx NanoSIMS element concentration profile (CPX1 zone A2). A traditional step function initial condition was used for this example. Vertical and horizontal gray lines call attention to the difference in timescale (dashed) that results from a small change in modeling temperature (solid)

Fig. 6 Density curves of diffusion coefficients (D) calculated with or without accounting for the covariance of  $D_0$  and E. Note that both methods capture similar median values; however, the extremely long tail of the "without covariance" curve illustrates the artificial broadening of possible Ds that occurs when  $D_0$  and E values are improperly paired (see "Sources of error" for further discussion)

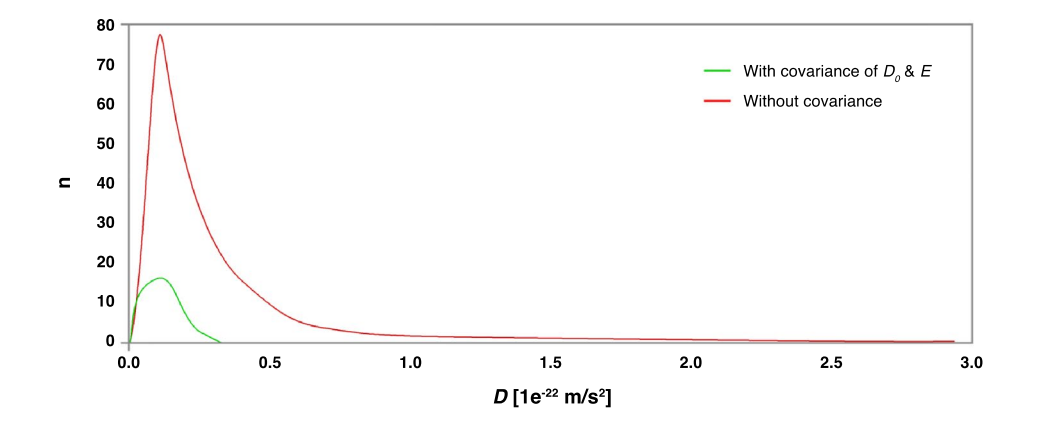
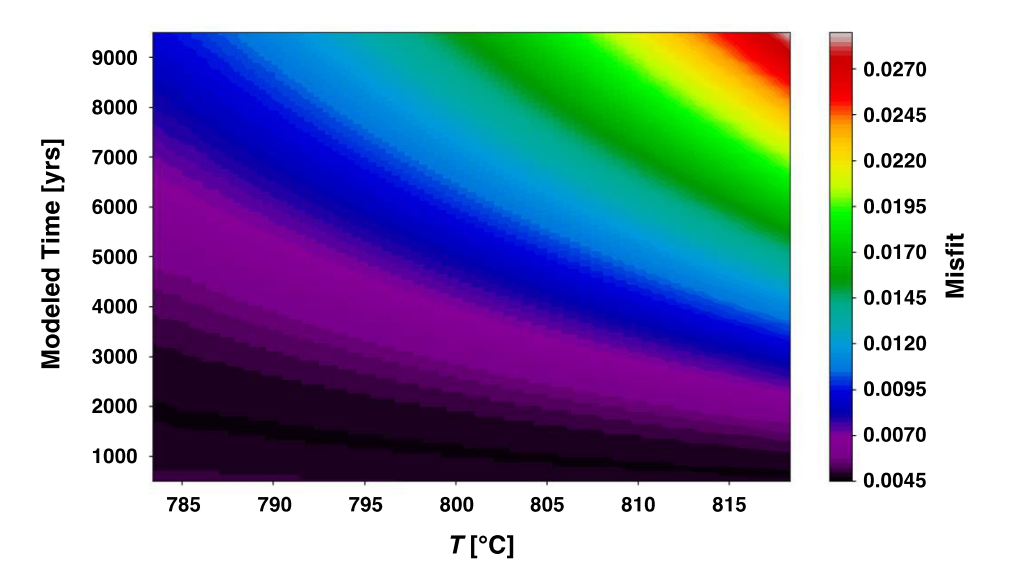




Fig. 8 Time vs. temperature (T) heatmap showing lowest misfit as darker colors. This plot was produced by modeling only the propagation of T error, which was determined by the geothermometer's error ( $\pm 20$  °C; Brugman and Till 2019). Note that although there is a best time for the modeled T of 800 °C, there are other times that represent equally good fits within the range of Ts shown on this figure



is generally one lowest value for the *misfit* between the modeled and measured profile, multiple temperature—time pairs may produce model profiles that yield the same misfit value (Fig. 8, black region).

This result highlights a fundamental principle underlying diffusion modeling: there is no single "best time" for a given elemental diffusion profile. There is a single best fit profile (a shape that produces the lowest misfit), but that profile can be arrived at via any number of degenerate combinations of t and D, of which T is a variable. Although a single time for a profile cannot be determined, it is possible to identify a region of qualifying solutions (Fig. 8, black region) and then constrain the timescales represented therein using known ages of temporally adjacent eruptions, as well as logic based on observed petrographic relationships and geothermometry.

#### **Recommendations for error reporting**

Modeling using (at minimum) a distribution of Ds based on propagating the T error reported by the geothermometer gives the maximum possible error envelope that is reasonably constrained and that may be used to compare timescales from different minerals, lavas, or magmatic systems that are modeled using different methods. Propagating all D error contributors  $(E, D_0, \text{ and } T)$  allows for comparison of timescales modeled using the same method. This tiered approach is modeled after that used by the geochronology community (Horstwood et al. 2016). Modeling diffusion from a step-function initial condition while propagating Terror is recommended to find a probable upper limit on error (as shown in Fig. 5 panels 1-3), as this method will produce the likely maximum timescale possible for the measured profile—although the true relevance of this value depends on whether the profile is partially the result of crystal growth.

Expressing uncertainty as asymmetric confidence intervals are necessitated by the nature of the curve that is being fit and the Arrhenius relationship between T and D, as well as the diffusive relaxation process being modeled. In diffusion chronometry, when the results are presented as PDFs, they are not perfect bell curves (Online Resource 5). These PDFs tend to have a higher value in the tail that approaches timescales of zero years, reflecting the possibility that no analytically resolvable diffusion took place. Often probability represented by the other tail will approach but not reach a misfit of zero. This is because for a model run in a wellconstrained time range, the plateau extrema (points at the beginning and end of the profile) and ramp midpoint for the modeled profile (Fig. 1) are likely to always match closely those of the measured concentration profile. See Online Resource 4 for further detail.

We recommend reporting timescale uncertainty in the form of asymmetric 95% confidence intervals clipped to the highest maximum timescale in the appropriate timescale bin (Fig. 5 panels 2–3, red and blue lines). This is the convention we have followed in "Diffusion modeling results" and Fig. 5 panels 6–7.

# Implications for the Scaup Lake rhyolite

The most recent magmatic events recorded by minerals in the SCL rhyolite are of interest because it is possible these events led to its eruption 220 kyr after the early UBM sequence (Fig. 2b). During long periods of quiescence, cooled magma bodies may exist as a near-solidus mush containing > 50% crystals (e.g., Hildreth 2004; Cooper and Kent 2014; Rubin et al. 2017). To become eruptible, the magma body must be rejuvenated, e.g., remelted by the addition of



heat or volatiles and/or less evolved magma. Rejuvenation can be identified via disequilibrium textures, such as the aforementioned intracrystalline compositional zonation. In this section we discuss our cpx findings in the context of the magmatic history of the Scaup Lake rhyolite.

## Crystal-melt equilibria

At SCL, we see abundant evidence of late-stage disequilibrium as represented by reverse zoning in the cpx (Fig. 3), sanidine (Till et al. 2015), and zircon (Bindeman and Valley 2001; Bindeman et al. 2008) as well as oscillatory zoning, resorbed cores, and truncation of zones that indicate previous dissolution. Some SCL cpx also have core exsolution lamellae that suggest a past period of disequilibrium. However, cpx crystals are euhedral, indicating that they were in equilibrium with the melt in the final stages of their magmatic residence time. Previous experimental studies indicate a  $K_{d_{SiO_2}}^{\text{cpx-liquid}} < 0.75$  for cpx in equilibrium with rhyolitic magma (Brugman and Till 2019). SCL analyses yield  $K_{d\text{SiO}_2}^{\text{cpx-liquid}} = 0.66$ , suggesting equilibrium. If SCL cpx were not in equilibrium with the melt, experimental dissolution rates of cpx in basaltic systems  $(1.05 \times 10^{-8} \text{ m/s at } 1250 \text{ }^{\circ}\text{C})$ and 0.5 GPa) suggest that the cpx would have disappeared from SCL's magma body within a few years (Chen and Zhang 2009).

# Comparison of SCL clinopyroxene and sanidine

To investigate the timing of the last events recorded by minerals before eruption, we sought to determine whether the SCL cpx show rejuvenation–eruption timescales consistent with the history recorded by SCL sanidine. SCL geothermometry and experimental studies on similar composition systems indicate that cpx crystallizes at or below the onset of sanidine stability (Bolte et al. 2015; Befus and Gardner 2016; Brugman and Till 2019). Therefore, it is possible for these minerals to have overlapping stability fields. Indeed, cpx-liquid geothermometry produces cpx rim temperatures of  $800 \pm 20$  °C and 2-feldspar thermometry gives sanidine rim temperatures of  $819 \pm 20$  °C (Elkins and Grove 1990; Wen and Nekvasil 1994; Brugman and Till 2019 and references therein), confirming that these two minerals likely co-crystallized and therefore potentially recorded the same changes in magma body conditions.

Prior work by Till et al. (2015) on sanidine from SCL noted similar widths of profiles from elements with different diffusivities (Ba, Sr, Mg), which suggested the profiles were a result of growth-then-diffusion. Using both feldspar growth rates and traditional step function initial

condition diffusion modeling, Till et al. (2015) reported two populations of sanidine rejuvenation-eruption times: 1.5–10 months and 10–40 years (Fig. 5 panel 9), which are short but consistent with models of eruptive timescales initiated by near-liquidus intrusions (Simakin and Bindeman 2012).

As shown in Fig. 5, the youngest SCL cpx rim timescale is  $\leq$  1000 years (panel 8)—much longer than the SCL sanidine timescales (panel 9). For this cpx timescale, denoted "Event 3" (Fig. 5 panel 8), to yield the same timescale as the oldest reported SCL sanidine timescale (10–40 years), the cpx diffusivity would have to be > 37 times faster. Although this is not impossible, it seems unlikely given the points discussed above (see "Diffusion coefficients used in modeling"). While it is possible that Event 3, which is a maximum, could encompass the SCL sanidine 10-40 years timescale, we think it is more likely that these are separate events, due to the location of these zones and the host crystals' growth rates. Sanidine growth in rhyolitic systems occurs at  $10^{-8}$ – $10^{-12}$  m/s (Swanson 1977), and so the thick rim (~500 µm) observed in these minerals could have grown on the order of days (Till 2017). Additionally, feldspar geothermometry indicates a 20-50 °C heating trend from core to rim (Till 2017) that is not replicated in the cpx rims. The thickness of the outermost sanidine rims and apparent change in recorded temperature may be the result of degassing-driven crystallization, likely associated with ascent (Humphreys et al. 2016; Till 2017), indicating that the growth of this thick outer rim was the result of a very late event recorded by the sanidine.

But for the cpx, the distance between the modeled rim zone boundary and crystal edge is much shorter  $(\sim 20-70 \mu m)$ , possibly due to slow growth of the mineral at these conditions. Cpx growth in basaltic systems is  $\sim 10^{-9}$  m/s, but is expected to be slower in lower-temperature systems as kinetic processes slow down and the system approaches the solidus (Orlando et al. 2008). Experiments and geothermometry confirm cpx was stable at 800 °C (Almeev et al. 2012; Gardner et al. 2014; Iacovino et al. 2015; Bolte et al. 2015; Befus and Gardner 2016; Brugman and Till 2019), but whether cpx is able to grow fast enough at the lower end of its stability field to record variable chemistry at the spatial resolution of existing analytical techniques is unknown. Therefore, the simplest explanation is that 10-40 years before SCL erupted, when the sanidine began recording ascent-related crystallization in the form of a 500 µm-thick rim, cpx was growing slowly enough that a similarly thick rim did not develop, leaving its outermost zones only a few 10s of μm from the crystal edge. As a result, any increase in cpx size from this late event is undetectable given the spatial resolution of our current analytical methods.



# Scaup Lake rhyolite history

The cpx and sanidine of SCL display a complex magmatic history of periodic disequilibria and heating events. Although it is possible that phenocrysts from these two mineral types record distinct magmatic histories in the more than decades before eruption, the lack of other evidence for final stage magma mixing suggests it is more likely that the chemical changes recorded in SCL cpx and sanidine are the result of multiple rejuvenation events of less evolved magma and subsequent differences in crystal growth rates at the relevant temperatures. This is indicated by reverse zoning in both minerals' rims and evidence of prior crystal dissolution.

Our cpx diffusion results suggest that for the zonation studied herein, the first of these rejuvenation events occurred ca. 5000 years before eruption, followed by a minimum of two events ca. 1000 and ≤ 1000 years before eruption. SCL sanidine suggests a minimum of two additional rejuvenation events at 10–40 years and < 10 months prior to eruption, the last of which likely triggered the eruption of SCL. This model of multiple rejuvenations and priming before an eruption is observed in other rhyolitic systems (Shane et al. 2008; Andersen et al. 2017; Allan et al. 2017; Szymanowski et al. 2017) as well as in more mafic systems (e.g., Ruth et al. 2018). Because SCL erupted ~ 220 ka after the previous early UBM eruptions, we suggest that each incremental rejuvenation event added a relatively small amount of material/ heat until the SCL magma body became eruptible (<~40% crystals depending on the physical parameters of a given system; Gelman et al. 2013), critical overpressure was reached, and the magma began to ascend and degas. This triggered degassing-driven rapid crystallization in the sanidine (Till 2017) while cpx growth was significantly more sluggish.

#### **Conclusions**

The method presented in this work is a powerful tool for diffusion studies on systems where crystals have experienced growth-then-diffusion, a process that is likely to occur in lower-temperature, more viscous, rhyolitic systems. We find that for SCL, cpx and sanidine crystal rims recorded multiple rejuvenation events over the > 5000 years before its eruption was triggered, the last rejuvenation event being < 10 months before eruption. This multiplicity indicates that there need not be a one-to-one relationship between a rejuvenation event and a volcanic eruption. Our results are important because—particularly for high-silica systems that may erupt explosively—the amount of time it takes for a quiescent magma body to become eruptible informs our models of magma body dynamics and storage conditions, and also has implications for volcano monitoring and hazard management.

Our comparison of maximum and best timescales for the same profiles (Fig. 5 panels 2–5) provides a cautionary tale for researchers who use a traditional step function when modeling diffusion in systems for which this initial condition may be contraindicated. Our results suggest that when growth-then-diffusion profiles are modeled using a traditional step function initial condition, the maximum times yielded by that method do not have a predictable relationship to the actual range of best times for the recorded event. Consequently, maximum times could be used to mistakenly assign ages to recorded events that are an order of magnitude too old. Similarly, we emphasize that there is no single "best time" that may be definitively attached to a given elemental diffusion profile. A modeled profile shape may be the best fit to a measured elemental profile; however, it can be produced by near-infinite degenerate combinations of time and the diffusion coefficient. Regarding the latter, further study of the rate of Fe-Mg diffusion in the low-Al, high-Fe cpx that is found in many high-silica magmatic systems is needed to more accurately model diffusion timescales in this mineral.

Given the above, a holistic petrologic approach must be used to constrain qualifying timescales to reasonable values. In addition to multiple-element-in-a-single-mineral approaches, our study highlights the value of conducting diffusion chronometry utilizing multiple elements in multiple mineral phases. Because each mineral's crystallization interval and growth rate constrain its ability to record magmatic events, an understanding of the phase equilibria, thermal history, and crystal growth rates/laws are thus also essential to interpreting the results of diffusion modeling. It is important to recognize that timescales much younger than 1000 years are not represented in SCL cpx possibly because crystal growth was so slow at ≤ 800 °C that it had essentially halted, or the new zone is too narrow to be resolved by the spatial resolution of the EPMA or NanoSIMS. Experimental data to constrain the crystal growth rates of cpx in rhyolitic systems would greatly enrich this conversation.

We find that the outermost zones of SCL cpx and sanidine did not record the same last rejuvenation event, and so the last event recorded by SCL cpx was not the last event experienced by SCL's magma body. Thus, we emphasize that the last event we are able to measure in each mineral is not necessarily the last event experienced by the magmatic system.

**Supplementary Information** The online version contains supplementary material available at https://doi.org/10.1007/s00410-022-01926-5.

Acknowledgements The authors thank the associate editor Mark Ghiorso and Katy Chamberlain and an anonymous reviewer for questions and comments that helped to greatly improve this manuscript. The authors thank Michelle Aigner, Chelsea Allison, Scott Blake, Anna Brunner, Michael Edwards, Rick Hervig, Kayla Iacovino, Rolf Jansen, Hongyu Lai, Noah McLean, Cameron Mercer, Euan Mutch, Bob Myhill, Jessica Noviello, Hannah Shamloo, Matthijs Van Soest, Penny Wieser, and Axel Wittmann. The authors thank Jorge Vazquez



for the use of Scaup Lake samples and specially thank Mitchell Phillips and Jamie Shaffer. Samples were collected under Yellowstone National Park research permits YELL-2012-SCI-5950.

**Funding** This work was supported by the National Science Foundation (NSF) under Graduate Research Fellowship #026257-001 to K.B. and an NSF CAREER grant EAR-1654584 to C.B.T. The Arizona State University (ASU) SIMS and NanoSIMS facilities are supported by NSF award EAR-1819550. The EPMA facilities at ASU are in part supported by the National Nanotechnology Coordinated Infrastructure grant ECCS-1542160.

**Data availability** Clinopyroxene and glass analyses: EarthChem https://doi.org/10.26022/IEDA/112315.

**Code availability** A description of the code is provided in Online Resource 3.

#### **Declarations**

**Conflict of interest** The authors declare no conflicts of interest.

#### References

- Albert H, Costa F, Martí J (2015) Timing of magmatic processes and unrest associated with mafic historical monogenetic eruptions in Tenerife Island. J Petrol. https://doi.org/10.1093/petrology/egv058
- Albert H, Costa F, Di Muro A et al (2019) Magma interactions, crystal mush formation, timescales, and unrest during caldera collapse and lateral eruption at ocean island basaltic volcanoes (Piton de la Fournaise, La Réunion). Earth Planet Sci Lett 515:187–199. https://doi.org/10.1016/j.epsl.2019.02.035
- Allan ASR, Barker SJ, Millet M-A et al (2017) A cascade of magmatic events during the assembly and eruption of a super-sized magma body. Contrib Miner Petrol. https://doi.org/10.1007/ s00410-017-1367-8
- Allan ASR, Morgan DJ, Wilson CJN, Millet M-A (2013) From mush to eruption in centuries: assembly of the super-sized Oruanui magma body. Contrib Miner Petrol 166:143–164. https://doi.org/10.1007/s00410-013-0869-2
- Almeev RR, Bolte T, Nash BP et al (2012) High-temperature, low-H2O Silicic Magmas of the Yellowstone Hotspot: an Experimental Study of Rhyolite from the Bruneau-Jarbidge Eruptive Center, Central Snake River Plain, USA. J Petrol 53:1837–1866. https://doi.org/10.1093/petrology/egs035
- Andersen NL, Singer BS, Costa F et al (2018) Petrochronologic perspective on rhyolite volcano unrest at Laguna del Maule, Chile. Earth Planet Sci Lett 493:57–70. https://doi.org/10.1016/j.epsl. 2018.03.043
- Andersen NL, Singer BS, Jicha BR et al (2017) Pleistocene to holocene growth of a large upper crustal rhyolitic magma reservoir beneath the Active Laguna del Maule Volcanic Field, Central Chile. J Petrol 58:85–114. https://doi.org/10.1093/petrology/egx006
- Azough F, Freer R (2000) Iron diffusion in single-crystal diopside. Phys Chem Minerals 27:732–740
- Bachmann O, Bergantz GW (2006) Gas percolation in upper-crustal silicic crystal mushes as a mechanism for upward heat advection and rejuvenation of near-solidus magma bodies. J Volcanol Geoth Res 149:85–102. https://doi.org/10.1016/j.jvolgeores. 2005.06.002

- Befus KS, Gardner JE (2016) Magma storage and evolution of the most recent effusive and explosive eruptions from Yellow-stone Caldera. Contrib Miner Petrol. https://doi.org/10.1007/s00410-016-1244-x
- Bindeman IN, Fu B, Kita NT, Valley JW (2008) Origin and Evolution of Silicic Magmatism at Yellowstone Based on Ion Microprobe Analysis of Isotopically Zoned Zircons. J Petrol 49:163–193. https://doi.org/10.1093/petrology/egm075
- Bindeman IN, Valley JW (2001) Low-δ18O rhyolites from Yellowstone: magmatic evolution based on analyses of zircons and individual phenocrysts. J Petrol 42:1491–1517
- Bolte T, Holtz F, Almeev R, Nash B (2015) The Blacktail Creek Tuff: an analytical and experimental study of rhyolites from the Heise volcanic field, Yellowstone hotspot system. Contrib Miner Petrol. https://doi.org/10.1007/s00410-015-1112-0
- Bouvet de Maisonneuve C, Costa F, Huber C et al (2016) How do olivines record magmatic events? Insights from major and trace element zoning. Contrib Miner Petrol. https://doi.org/10.1007/s00410-016-1264-6
- Brugman K, Till CB, Bose M (2022) Clinopyroxene and glass compositions (EPMA) from the Scaup Lake rhyolite, Yellowstone-Caldera, EarthChem, 1.0, https://doi.org/10.26022/IEDA/112315
- Brugman KK, Till CB (2019) A low-aluminum clinopyroxene-liquid geothermometer for high-silica magmatic systems. Am Miner 104:996–1004. https://doi.org/10.2138/am-2019-6842
- Chamberlain KJ, Morgan DJ, Wilson CJN (2014) Timescales of mixing and mobilisation in the Bishop Tuff magma body: perspectives from diffusion chronometry. Contrib Miner Petrol. https://doi.org/10.1007/s00410-014-1034-2
- Chen Y, Zhang Y (2009) Clinopyroxene dissolution in basaltic melt. Geochim Cosmochim Acta 73:5730–5747. https://doi.org/10.1016/j.gca.2009.06.016
- Christiansen RL (2001) The Quaternary and Pliocene Yellowstone Plateau volcanic field of Wyoming, Idaho, and Montana. U.S. Geological Survey, Reston, VA
- Christiansen RL, Lowenstern JB, Smith RB et al (2007) Preliminary Assessment of Volcanic and Hydrothermal Hazards in Yellowstone National Park and Vicinity. USGS
- Cooper GF, Morgan DJ, Wilson CJN (2017) Rapid assembly and rejuvenation of a large silicic magmatic system: insights from mineral diffusive profiles in the Kidnappers and Rocky Hill deposits, New Zealand. Earth Planet Sci Lett 473:1–13. https://doi.org/10.1016/j.epsl.2017.05.036
- Cooper KM, Kent AJR (2014) Rapid remobilization of magmatic crystals kept in cold storage. Nature 506:480–483. https://doi. org/10.1038/nature12991
- Costa F, Chakraborty S (2004) Decadal time gaps between mafic intrusion and silicic eruption obtained from chemical zoning patterns in olivine. Earth Planet Sci Lett 227:517–530. https://doi.org/10.1016/j.epsl.2004.08.011
- Costa F, Dungan M (2005) Short time scales of magmatic assimilation from diffusion modeling of multiple elements in olivine. Geology 33:837-840
- Costa F, Morgan D (2011) Time constraints from chemical equilibration in magmatic crystals. Timescales of magmatic processes: from core to atmosphere, 1st edn. Blackell Publishing Ltd, pp 123–159
- Costa F, Chakraborty S, Dohmen R (2003) Diffusion coupling between trace and major elements and a model for calculation of magma residence times using plagioclase. Geochim Cosmochim Acta 67:2189–2200
- Costa F, Dohmen R, Chakraborty S (2008) Time scales of magmatic processes from modeling the zoning patterns of crystals. Rev Mineral Geochem 69:545–594. https://doi.org/10.2138/rmg. 2008.69.14



- Costa F, Shea T, Ubide T (2020) Diffusion chronometry and the timescales of magmatic processes. Nat Rev Earth Environ 1:201–214. https://doi.org/10.1038/s43017-020-0038-x
- Couperthwaite FK, Morgan DJ, Pankhurst MJ et al (2021) Reducing epistemic and model uncertainty in ionic inter-diffusion chronology: a 3D observation and dynamic modeling approach using olivine from Piton de la Fournaise, La Réunion. Am Miner 106:481–494. https://doi.org/10.2138/am-2021-7296CCBY
- Devoir A, Bloch E, Müntener O (2021) Residence time of igneous garnet in Si-rich magmatic systems: insights from diffusion modeling of major and trace elements. Earth Planet Sci Lett 560:13. https://doi.org/10.1016/j.epsl.2021.116771
- Dimanov A, Wiedenbeck M (2006) (Fe, Mn)-Mg interdiffusion in natural diopside: effect of pO2. Eur J Mineral 18:705–718. https://doi.org/10.1127/0935-1221/2006/0018-0705
- Druitt TH, Costa F, Deloule E et al (2012) Decadal to monthly timescales of magma transfer and reservoir growth at a caldera volcano. Nature 482:77–80. https://doi.org/10.1038/nature10706
- Elkins LT, Grove TL (1990) Ternary feldspar experiments and thermodynamic models. Am Miner 75:544–559
- Fabbro GN, Druitt TH, Costa F (2017) Storage and eruption of silicic magma across the transition from dominantly effusive to calderaforming states at an Arc Volcano (Santorini, Greece). J Petrol 58:2429–2464. https://doi.org/10.1093/petrology/egy013
- Flaherty T, Druitt TH, Tuffen H et al (2018) Multiple timescale constraints for high-flux magma chamber assembly prior to the Late Bronze Age eruption of Santorini (Greece). Contrib Miner Petrol. https://doi.org/10.1007/s00410-018-1490-1
- Gardner JE, Befus KS, Gualda GAR, Ghiorso MS (2014) Experimental constraints on rhyolite-MELTS and the Late Bishop Tuff magma body. Contrib Miner Petrol. https://doi.org/10.1007/s00410-014-1051-1
- Gelman SE, Gutiérrez FJ, Bachmann O (2013) On the longevity of large upper crustal silicic magma reservoirs. Geology 41:759–762. https://doi.org/10.1130/G34241.1
- Girard G, Stix J (2012) Future volcanism at Yellowstone caldera: Insights from geochemistry of young volcanic units and monitoring of volcanic unrest. GSA Today. https://doi.org/10.1130/GSATG143A.1
- Girard G, Stix J (2009) Magma recharge and crystal mush rejuvenation associated with early post-collapse upper basin member rhyolites, Yellowstone Caldera, Wyoming. J Petrol 50:2095–2125. https://doi.org/10.1093/petrology/egp070
- Girard G, Stix J (2010) Rapid extraction of discrete magma batches from a large differentiating magma chamber: the Central Plateau Member rhyolites, Yellowstone Caldera, Wyoming. Contrib Miner Petrol 160:441–465. https://doi.org/10.1007/s00410-009-0487-1
- Gordeychik B, Churikova T, Kronz A et al (2018) Growth of, and diffusion in, olivine in ultra-fast ascending basalt magmas from Shiveluch volcano. Sci Rep. https://doi.org/10.1038/s41598-018-30133-1
- Gualda GAR, Pamukcu AS, Ghiorso MS et al (2012) Timescales of quartz crystallization and the longevity of the bishop giant magma body. PLoS ONE 7:e37492. https://doi.org/10.1371/journ al.pone.0037492
- Gualda GAR, Sutton SR (2016) The year leading to a supercruption. PLoS ONE 11:e0159200. https://doi.org/10.1371/journal.pone. 0159200
- Hartley ME, Morgan DJ, Maclennan J et al (2016) Tracking timescales of short-term precursors to large basaltic fissure eruptions through Fe–Mg diffusion in olivine. Earth Planet Sci Lett 439:58–70. https://doi.org/10.1016/j.epsl.2016.01.018
- Hildreth W (2004) Volcanological perspectives on Long Valley, Mammoth Mountain, and Mono Craters: several contiguous but

- discrete systems. J Volcanol Geoth Res 136:169–198. https://doi.org/10.1016/j.jvolgeores.2004.05.019
- Horstwood MSA, Košler J, Gehrels G et al (2016) Community-derived standards for LA-ICP-MS U-(Th-)Pb geochronology uncertainty propagation, age interpretation and data reporting. Geostand Geoanal Res 40:311–332. https://doi.org/10.1111/j. 1751-908X.2016.00379.x
- Humphreys MCS, Edmonds M, Klöcking MS (2016) The validity of plagioclase-melt geothermometry for degassing-driven magma crystallization. Am Miner 101:769–779. https://doi.org/10. 2138/am-2016-5314
- Iacovino K, Kim JS, Sisson TW et al (2015) New constraints on the geochemistry of the millennium eruption of Mount Paektu (Changbaishan), Democratic People's Republic of Korea/ China. In: 2015 AGU Fall Meeting. San Francisco, CA, USA
- Jollands MC (2020) Assessing analytical convolution effects in diffusion studies: applications to experimental and natural diffusion profiles. PLoS ONE 15:e0241788. https://doi.org/10.1371/ journal.pone.0241788
- Kent A, Till C, Cooper K (2020) Studying the initiation of volcanic eruptions: time for a petrological perspective. EarthArXiv. https://doi.org/10.31223/X5S01X
- Loewen MW, Bindeman IN (2015) Oxygen isotope and trace element evidence for three-stage petrogenesis of the youngest episode (260–79 ka) of Yellowstone rhyolitic volcanism. Contrib Miner Petrol. https://doi.org/10.1007/s00410-015-1189-5
- Lynn KJ, Garcia MO, Shea T et al (2017) Timescales of mixing and storage for Keanakāko'i Tephra magmas (1500–1820 C.E.), Kīlauea Volcano, Hawai'i. Contrib Mineral Petrol. https://doi. org/10.1007/s00410-017-1395-4
- Magee R, Ubide T, Kahl M (2020) The lead-up to Mount Etna's most destructive historic eruption (1669). Cryptic recharge recorded in clinopyroxene. J Petrol 61:25. https://doi.org/10.1093/petrology/egaa025
- Mahood G, Hildreth W (1983) Large partition coefficients for trace elements in high-silica rhyolites. Geochim Cosmochim Acta 47:11–30
- Martin VM, Morgan DJ, Jerram DA et al (2008) Bang! month-scale eruption triggering at Santorini Volcano. Science 321:1178–1178. https://doi.org/10.1126/science.1159584
- Matthews NE, Vazquez JA, Calvert AT (2015) Age of the Lava Creek supereruption and magma chamber assembly from combined <sup>40</sup> Ar/ <sup>39</sup> Ar and U-Pb dating of sanidine and zircon crystals. Geochem Geophys Geosyst 16:2508–2528. https://doi.org/10.1002/2015GC005881
- Milman-Barris MS, Beckett JR, Baker MB et al (2008) Zoning of phosphorus in igneous olivine. Contrib Miner Petrol 155:739–765. https://doi.org/10.1007/s00410-007-0268-7
- Mollo S, Del Gaudio P, Ventura G et al (2010) Dependence of clinopyroxene composition on cooling rate in basaltic magmas: Implications for thermobarometry. Lithos 118:302–312. https://doi.org/10.1016/j.lithos.2010.05.006
- Morgado E, Morgan DJ, Castruccio A et al (2019) Old magma and a new, intrusive trigger: using diffusion chronometry to understand the rapid-onset Calbuco eruption, April 2015 (Southern Chile). Contrib Miner Petrol. https://doi.org/10.1007/s00410-019-1596-0
- Morgan DJ, Blake S (2006) Magmatic residence times of zoned phenocrysts: introduction and application of the binary element diffusion modelling (BEDM) technique. Contrib Miner Petrol 151:58–70. https://doi.org/10.1007/s00410-005-0045-4
- Morgan DJ, Blake S, Rogers NW et al (2004) Time scales of crystal residence and magma chamber volume from modelling of diffusion profiles in phenocrysts: Vesuvius 1944. Earth Planet Sci Lett 222:933–946. https://doi.org/10.1016/j.epsl.2004.03.030



- Moussallam Y, Rose-Koga EF, Koga KT et al (2019) Fast ascent rate during the 2017–2018 Plinian eruption of Ambae (Aoba) volcano: a petrological investigation. Contrib Miner Petrol. https://doi.org/10.1007/s00410-019-1625-z
- Müller T, Dohmen R, Becker HW et al (2013) Fe–Mg interdiffusion rates in clinopyroxene: experimental data and implications for Fe–Mg exchange geothermometers. Contrib Miner Petrol 166:1563–1576. https://doi.org/10.1007/s00410-013-0941-y
- Mutch EJF, Maclennan J, Shorttle O et al (2019) Rapid transcrustal magma movement under Iceland. Nat Geosci. https://doi.org/10.1038/s41561-019-0376-9
- Mutch EJF, Maclennan J, Shorttle O et al (2021) DFENS: diffusion chronometry using finite elements and nested sampling. Geochem Geophys Geosyst. https://doi.org/10.1029/2020GC009303
- Myers ML, Wallace PJ, Wilson CJN et al (2016) Prolonged ascent and episodic venting of discrete magma batches at the onset of the Huckleberry Ridge supereruption, Yellowstone. Earth Planet Sci Lett 451:285–297. https://doi.org/10.1016/j.epsl.2016.07.023
- Newcombe ME, Plank T, Barth A et al (2020) Water-in-olivine magma ascent chronometry: every crystal is a clock. J Volcanol Geoth Res 398:106872. https://doi.org/10.1016/j.jvolgeores.2020. 106872
- Orlando A, D'Orazio M, Armienti P, Borrini D (2008) Experimental determination of plagioclase and clinopyroxene crystal growth rates in an anhydrous trachybasalt from Mt Etna (Italy). Eur J Mineral 20:653–664. https://doi.org/10.1127/0935-1221/2008/0020-1841
- Pamukcu AS, Ghiorso MS, Gualda GAR (2016) High-Ti, bright-CL rims in volcanic quartz: a result of very rapid growth. Contrib Miner Petrol. https://doi.org/10.1007/s00410-016-1317-x
- Petrone CM, Braschi E, Francalanci L et al (2018) Rapid mixing and short storage timescale in the magma dynamics of a steady-state volcano. Earth Planet Sci Lett 492:206–221. https://doi.org/10.1016/j.epsl.2018.03.055
- Pistone M, Blundy J, Brooker RA (2017) Water transfer during magma mixing events: insights into crystal mush rejuvenation and melt extraction processes. Am Miner 102:766–776. https://doi.org/10.2138/am-2017-5793
- Prissel KB, Krawczynski MJ, Van Orman JA (2020) Fe–Mg and Fe–Mn interdiffusion in ilmenite with implications for geospeedometry using oxides. Contrib Mineral Petrol 175:17. https://doi.org/10.1007/s00410-020-01695-z
- Pritchard CJ, Larson PB (2012) Genesis of the post-caldera eastern Upper Basin Member rhyolites, Yellowstone, WY: from volcanic stratigraphy, geochemistry, and radiogenic isotope modeling. Contrib Miner Petrol 164:205–228. https://doi.org/10.1007/s00410-012-0733-9
- Reid MR, Vazquez JA (2017) Fitful and protracted magma assembly leading to a giant eruption, Youngest Toba Tuff, Indonesia. Geochem Geophys Geosyst 18:156–177. https://doi.org/10.1002/2016GC006641
- Rivera TA, Schmitz MD, Crowley JL, Storey M (2014) Rapid magma evolution constrained by zircon petrochronology and 40Ar/39Ar sanidine ages for the Huckleberry Ridge Tuff, Yellowstone, USA. Geology 42:643–646. https://doi.org/10.1130/G35808.1
- Rivera TA, Schmitz MD, Jicha BR, Crowley JL (2016) Zircon Petrochronology and 40Ar/ 39Ar Sanidine Dates for the Mesa Falls Tuff: crystal-scale records of magmatic evolution and the short lifespan of a large Yellowstone magma chamber. J Petrol 57:1677–1704. https://doi.org/10.1093/petrology/egw053
- Rubin A, Cooper KM, Leever M et al (2016) Changes in magma storage conditions following caldera collapse at Okataina Volcanic Center, New Zealand. Contrib Miner Petrol. https://doi.org/10.1007/s00410-015-1216-6

- Rubin A, Cooper KM, Till CB et al (2017) Rapid cooling and cold storage in a silicic magma reservoir recorded in individual crystals. Science 356:1154–1156
- Ruth DCS, Costa F, Bouvet de Maisonneuve C et al (2018) Crystal and melt inclusion timescales reveal the evolution of magma migration before eruption. Nat Commun. https://doi.org/10.1038/ s41467-018-05086-8
- Salviulo G, Secco L, Marzoli A et al (2000) Ca-rich pyroxene from basic and silicic volcanic rocks from the Cameroon Volcanic Line (West-Africa): crystal chemistry and petrological relationships. Mineral Petrol 70:73–88. https://doi.org/10.1007/s0071 00070014
- Shamloo HI, Till CB (2019) Decadal transition from quiescence to supereruption: petrologic investigation of the Lava Creek Tuff, Yellowstone Caldera, WY. Contrib Mineral Petrol. https://doi.org/10.1007/s00410-019-1570-x
- Shane P, Smith VC, Nairn I (2008) Millennial timescale resolution of rhyolite magma recharge at Tarawera volcano: insights from quartz chemistry and melt inclusions. Contrib Mineral Petrol 156:397–411. https://doi.org/10.1007/s00410-008-0292-2
- Simakin AG, Bindeman IN (2012) Remelting in caldera and rift environments and the genesis of hot, "recycled" rhyolites. Earth Planet Sci Lett 337–338:224–235. https://doi.org/10.1016/j.epsl. 2012.04.011
- Singer BS, Costa F, Herrin JS et al (2016) The timing of compositionally-zoned magma reservoirs and mafic 'priming' weeks before the 1912 Novarupta-Katmai rhyolite eruption. Earth Planet Sci Lett 451:125–137. https://doi.org/10.1016/j.epsl.2016.07.015
- Sisson TW (1991) Pyroxene-high silica rhyolite trace element partition coefficients measured by ion microprobe. Geochim Cosmochim Acta 55:1575–1585. https://doi.org/10.1016/0016-7037(91) 90129-S
- Stelten ME, Cooper KM, Vazquez JA et al (2015) Mechanisms and timescales of generating eruptible rhyolitic magmas at Yellow-stone Caldera from zircon and sanidine geochronology and geochemistry. J Petrol 56:1607–1642. https://doi.org/10.1093/petrology/egy047
- Stelten ME, Cooper KM, Wimpenny JB et al (2017) The role of mantle-derived magmas in the isotopic evolution of Yellowstone's magmatic system. Geochem Geophys Geosyst 18:1350–1365. https://doi.org/10.1002/2016GC006664
- Stelten ME, Champion DE, Kuntz MA (2018) The timing and origin of pre- and post-caldera volcanism associated with the Mesa Falls Tuff, Yellowstone Plateau volcanic field. J Volcanol Geoth Res 350:47–60. https://doi.org/10.1016/j.jvolgeores.2017.12.002
- Stock MJ, Humphreys MCS, Smith VC et al (2016) Late-stage volatile saturation as a potential trigger for explosive volcanic eruptions. Nat Geosci 9:249–254. https://doi.org/10.1038/ngeo2639
- Sundermeyer C, Di Muro A, Gordeychik B, Wörner G (2020) Time-scales of magmatic processes during the eruptive cycle 2014–2015 at Piton de la Fournaise, La Réunion, obtained from Mg–Fe diffusion modelling in olivine. Contrib Miner Petrol. https://doi.org/10.1007/s00410-019-1642-y
- Swanson SE (1977) Relation of nucleation and crystal-growth rate to the development of granitic textures. Am Miner 62:966–978
- Szymanowski D, Wotzlaw J-F, Ellis BS et al (2017) Protracted nearsolidus storage and pre-eruptive rejuvenation of large magma reservoirs. Nature Geosci 10:777–782. https://doi.org/10.1038/ ngeo3020
- Till CB (2017) An integrated approach for identifying P-T-X-t Histories and eruption triggers for silicic magmas; an example examining the scaup lake Rhyolite Yellowstone Caldera, WY. In: 2017 Scientific Assembly. Portland, OR
- Till CB, Vazquez JA, Boyce JW (2015) Months between rejuvenation and volcanic eruption at Yellowstone caldera, Wyoming. Geology 43:695–698. https://doi.org/10.1130/G36862



- Till CB, Vazquez JA, Stelten ME et al (2019) Coexisting discrete bodies of rhyolite and punctuated volcanism characterize Yellowstone's Post-Lava Creek Tuff Caldera Evolution. Geochem Geophys Geosyst 20:3861–3881. https://doi.org/10.1029/2019G C008321
- Van Orman JA, Grove TL, Shimizu N (2001) Rare earth element diffusion in diopside: influence of temperature, pressure, and ionic radius, and an elastic model for diffusion in silicates. Contrib Miner Petrol 141:687–703. https://doi.org/10.1007/s004100100 269
- Vazquez JA, Kyriazis SF, Reid MR et al (2009) Thermochemical evolution of young rhyolites at Yellowstone: evidence for a cooling but periodically replenished postcaldera magma reservoir. J Volcanol Geoth Res 188:186–196. https://doi.org/10.1016/j.jvolgeores.2008.11.030
- Watts KE, Bindeman IN, Schmitt AK (2012) Crystal scale anatomy of a dying supervolcano: an isotope and geochronology study of individual phenocrysts from voluminous rhyolites of the

- Yellowstone caldera. Contrib Miner Petrol 164:45–67. https://doi.org/10.1007/s00410-012-0724-x
- Wen S, Nekvasil H (1994) SOLVALC: an interactive graphics program package for calculating the ternary feldspar solvus and for two-feldspar geothermometry. Comput Geosci 20:1025–1040. https://doi.org/10.1016/0098-3004(94)90039-6
- Wotzlaw J-F, Bindeman IN, Stern RA et al (2015) Rapid heterogeneous assembly of multiple magma reservoirs prior to Yellowstone supereruptions. Sci Rep 5:14026. https://doi.org/10.1038/srep1 4026
- Zhang Y (2008) Geochemical kinetics. Princeton University Press, Princeton, New Jersey

**Publisher's Note** Springer Nature remains neutral with regard to jurisdictional claims in published maps and institutional affiliations.

